International Journal of Solids and Structures 49 (2012) 3883–3900

Contents lists available at SciVerse ScienceDirect

International Journal of Solids and Structures

journal homepage: www.elsevier.com/locate/ijsolstr

The multiscale approach to the curing of polymers incorporating viscous and shrinkage effects

S. Klinge [a,*], A. Bartels [a], P. Steinmann [b]

[a] Institute of Mechanics, Ruhr-University Bochum, 44780 Bochum, Germany
[b] Chair of Applied Mechanics, University of Erlangen-Nuremberg, 91058 Erlangen, Germany

ARTICLE INFO

Article history:
Received 4 June 2012
Received in revised form 4 August 2012
Available online 28 August 2012

Keywords:
Polymer
Curing
Viscous effects
Multi-field potential
Multiscale FEM
Homogenization

ABSTRACT

This contribution deals with the modeling of viscoelastic and shrinkage effects accompanying the curing of polymers at multiple length scales. For the modeling of viscous effects, the deformation at the micro-level is decomposed into an elastic and a viscoelastic part, and a corresponding energy density consisting of equilibrium and non-equilibrium parts is proposed. The former is related to the total deformation; it has the form of a convolution integral and depends on the time evolution of the material parameters. The non-equilibrium part depends on the elastic part of deformations only. The material parameters are constant in time, thus an integral form is not necessary. In contrast to the viscous effects, the modeling of shrinkage effects does not require any further extension of the expression for the energy density, but an additional decomposition of the deformation into a shrinkage and a mechanical part. Since the material compressibility is taken into consideration, a multifield formulation is applied for the equilibrium as well as for the non-equilibrium energy part. As a final aspect, the paper includes a study of macroheterogenous polymers for whose modeling the multiscale finite element method is applied. Within this numerical approach, a macroscopic body is treated as a homogeneous body whose effective properties are evaluated on the basis of the simulations which are carried out at the level of the representative volume element. The application of the model proposed is illustrated on the basis of examples studying the influence of individual parameters on the stress state as well as the influence of the volume fraction of different phases at the microscale on the effective material behavior.

1. Introduction

Curing of polymers is a complex process having strong influence on the application range of this class of materials. At this stage, a liquid polymer gradually transforms into a viscoelastic solid which is caused by cross-linking of the initially short polymer chains. The present paper is in particular focused on the second stage of the curing process starting with the so called gel point. During this phase, the polymer is considered as the viscoelastic solid with the time evolving material properties whose experimental determination requires two groups of tests. The dynamic mechanical analysis (DMA) is used for the determination of the bulk and shear moduli and it shows that these two parameters have a zero initial value and that they are increasing very fast at the beginning of the curing process. However, the rates become moderate as the end of the curing process approaches so that parameters tend slowly towards their final values. Although measured by DMA, the values of the compression modulus that are lower than the compression modulus of the liquid polymer are commonly neglected (Kiasat, 2000; Kiasat, 2000a). In contrast to the shear and bulk moduli, the investigations of Poisson's ratio still do not yield a globally accepted scenario for the time evolution of this parameter. While some authors claim that this parameter changes from 0.40 to 0.34 with the peak at 0.45 (Tsou et al., 1995), the other sources indicate that this parameter gradually falls from 0.5 to 0.35 (Kiasat, 2000) or gradually increases from 0.4 to 0.5 (O'Brien et al., 2007). In spite of different numerical values all investigations indicate that the high values of Poisson's ratio (close to 0.5) are typical of the curing of polymers. Different from the elastic parameters, the viscosity of polymers is investigated on the basis of static tests showing a significant decrease of the relaxation modulus and a clear increase of the creep compliance during the corresponding tests. The static tests are also used for the study of the autogeneous decrease of the volume referred to as shrinkage. This phenomenon represents the main impediment for the manufacturing of the composite polymers since it causes the warpage and residual stresses.

The comprehensive overviews of mechanical models concerned with the simulation of polymers are presented in the works of Boyce and Arruda (2000) and Marckmann and Verron

* Corresponding author. Tel.: +49 (0) 234 32 26552; fax: +49 (0) 234 32 14154.
E-mail address: sandra.klinge@rub.de (S. Klinge).

0020-7683/$ - see front matter © 2012 Elsevier Ltd. All rights reserved.
http://dx.doi.org/10.1016/j.ijsolstr.2012.08.016

(2006) as well as in the introductory chapters in the works of Anand and Gurtin (2003), Hossain et al. (2009a,b), Klinge (2012) and Mulliken and Boyce (2006). Among others, the model of Hossain et al. (2009a) will be particularly mentioned here since it focuses on the curing phenomenon and is convenient for the implementation within a finite element approach. Within this model, the free energy density is assumed in the form of a convolution integral which enables the simulation of materials with the time-dependent material parameters. The model is furthermore extended in order to capture the viscous and shrinkage effects (Hossain et al., 2010) as well as the damage effects (Mergheim et al., 2012). It is also coupled with the Arruda–Boyce model for the purpose of modeling of a specific group of polymers (Hossain and Steinmann, 2011). However, the possible incompressibility of curing polymers is not taken into consideration here. This novel aspect is first introduced in the work considering the multifield formulation for the cumulative free energy density (Klinge, 2012). In this context, the displacements, the volume change and the hydrostatic pressure are introduced as the field variables, which guarantees that the effects of the volume locking are suppressed (Simo and Hughes, 1997). The mentioned work is also concerned with the modeling of microheterogeneous curing polymers based on the application of the multiscale finite element method (FEM) (Miehe et al., 2002; Feyel, 2003; Schroeder, 2000; Klinge and Hackl, 2012; Ilic and Hackl, 2009; Ilic, 2010). Due to the wide application of the reinforced polymers, this topic is of special interest. The multiscale FEM is a numerical homogenization approach in which a representative volume element (RVE) is chosen to depict the structure of the microheterogeneous polymer while a macroscopic test is carried out under the assumption that the material is homogeneous at this level. The so called effective values are calculated on the basis of the simulations carried out on the level of the RVE. While the mentioned work (Klinge, 2012) is focused on the modeling of curing in the assumption that it is an elastic process, the main intention in the current paper is to extend the multifield formulation by introducing new terms related to the viscous and shrinkage effects. The influence of these effects will also be studied in the case of composite polymers.

The relevant topics, namely the mechanical modeling and the homogenization technique, are presented within the current paper as follows. Section 2 gives an overview of the model for the purely elastic curing in which the free energy density is assumed as a convolution integral consisting of a volumetric and a deviatoric part (Klinge, 2012). The section also presents the underlying principles of the multiscale concept used for the modeling of microheterogeneous polymers. The incorporation of viscous effects is explained in Section 3. For this purpose, the total deformations is decomposed into elastic and viscoelastic part and a new energy part dependent only on the elastic part of deformation is introduced. Subsequently, the development of the corresponding finite element formulation and an illustrative example dealing with a neo-Hooke-type material are studied (Sections 4 and 5). The autogenous shrinkage is considered in Section 6. In contrast to viscous effects, no extension of the free energy density is here necessary but the deformation is decomposed into a shrinkage and a mechanical part. The proposed approach has a general character and the special cases such as the elastic or the viscoelastic curing can be obtained by zeroing the corresponding terms. The model is in particular suitable for implementation within the multiscale concept which enables the simulation of microheterogeneous polymers (Section 7). The results of numerical multiscale simulations are presented in Section 8. Here, the singlescale simulations are used to study the influence of particular parameters on the stress state while the multiscale evaluations are focused on the influence of the volume fraction of different phases on the effective behavior. The paper closes with a presentation of the conclusions and an outlook.

2. Previous work

2.1. Modeling curing polymers based on isochoric/volumetric decomposition

In our previous work (Klinge, 2012), the focus was placed on the basic issues of curing process, namely the evolution of elastic material parameters and the isochoric/volumetric decomposition. The model exposed, uses an assumption for the free energy density Φ in a three-field $(\mathbf{u}, \theta, p)$ formulation

$$\Phi(\mathbf{u},\theta,p) = \Phi_{\text{dev}}\{\Psi_{\text{dev}}(\mathbf{C}_{\text{iso}})\} + \Phi_{\text{vol}}\{\Psi_{\text{vol}}(\theta)\} + p[J(\mathbf{u}) - \theta], \tag{1}$$

where $\mathbf{u}$ denotes the deformation and represents the primary variable. The parentheses $(\cdot)$ are used to denote the dependency of a function on an argument and the curly brackets $\{\cdot\}$ indicate the dependency of a functional on a function. The square brackets do not appear here but will be applied in the classical sense to signify a different precedence of operators. The energy density (1) is decomposed into a deviatoric and a volumetric part depending on the corresponding strain energy densities Ψ_{dev} and Ψ_{vol}. Moreover, the deviatoric part is dependent on the isochoric part of the right Cauchy–Green deformation tensor $\mathbf{C}_{\text{iso}}$, while the volumetric part depends on the volume change θ. The Lagrange term is added as the last one and stipulates the equality of the Jacobian J with the volume change θ. The Lagrange multiplier p represents the hydrostatic pressure. The prescribed three-field formulation (Simo and Hughes, 1997) guarantees that the volume locking effects are circumvented.

The formulation (1) is furthermore completed by introducing the following assumptions for the individual parts of the free energy density

$$\Phi_{\text{dev}}(t) = \frac{1}{2}\int_0^t \left[\mathbb{C}'_{\text{dev}}(\tau) : [\mathbf{C}_{\text{iso}}(t) - \mathbf{C}_{\text{iso}}(\tau)]\right] : [\mathbf{C}_{\text{iso}}(t) - \mathbf{C}_{\text{iso}}(\tau)]\, d\tau, \tag{2}$$

$$\Phi_{\text{vol}}(t) = \frac{1}{2}\int_0^t K'(\tau)[\theta(t) - \theta(\tau)]^2 d\tau. \tag{3}$$

Here, τ is a time variable, the prime symbol is used to denote the following time derivatives $\mathbb{C}'_{\text{dev}}(\tau) = \frac{d\mathbb{C}_{\text{dev}}(\tau)}{d\tau}$, $K'(\tau) = \frac{dK(\tau)}{d\tau}$, and the convolution integrals are implemented in order to insert the influence of time-dependent material parameters. The free energy density in this model might be interpreted as the total, accumulated energy density while the strain energy densities Ψ_{dev} and Ψ_{vol} are related rather to the body response to the current state of deformations and are used to define the corresponding stiffnesses $\mathbb{C}_{dev}(t)$ and $K(t)$

$$\mathbb{C}_{\text{dev}}(t) = 4\frac{\partial^2 \Psi_{\text{dev}}(\mathbf{C}_{\text{iso}}(t))}{\partial \mathbf{C}^2(t)}, \tag{4}$$

$$K(t) = \frac{\partial^2 \Psi_{\text{vol}}(\theta(t))}{\partial \theta^2(t)}. \tag{5}$$

2.2. Multiscale approach for modeling the microheterogeneous polymers

Another important aspect exposed in our previous work is the simulation of microheterogeneous polymers on the basis of the multiscale FEM (Feyel, 2003; Feyel and Chaboche, 2000; Ilic and Hackl, 2009; Klinge and Hackl, 2012; Miehe et al., 2002; Schroeder, 2000).

The main feature of the mentioned approach is that the simulation of a heterogeneous body is decomposed into the solution of two boundary value problems (BVPs). One of them is related to the modeling of a macroscopic body based on effective material

properties and the other to the simulations of a representative volume element (RVE) depicting the material microstructure. The bonding of these two BVPs is achieved by the definitions for the macroscopic quantities as well as by the Hill macrohomogeneity condition (Hill, 1963, 1972), which is expressed in two ways

$$\overline{\mathbf{P}} : \dot{\overline{\mathbf{F}}} = \frac{1}{V}\int_V \mathbf{P} : \dot{\mathbf{F}} dV \quad \Longleftrightarrow \quad \frac{1}{V}\int_{\partial\mathcal{B}} \left[\mathbf{T} - \overline{\mathbf{P}}\mathbf{N}\right] \cdot \left[\dot{\mathbf{x}} - \dot{\overline{\mathbf{F}}}\mathbf{X}\right] dA = 0. \tag{6}$$

Here, the overbar symbol is used in order to distinguish macroscopic from microscopic quantities. The capital letters are related to the reference configuration and small letters to the current configuration. Typically of the theory of finite deformations: $\mathbf{x}$ and $\mathbf{X}$ are position vectors, $\mathbf{P}$ denotes the first Piola stress tensor, $\mathbf{T}$ is the traction vector, $\mathbf{N}$ the normal vector to the surface of the RVE $\mathcal{B}$.

The Hill condition (6) furthermore enables the determination of three basic types of boundary conditions for an RVE. However, only the periodic boundary conditions are applied within this work since the polymers with periodic microstructure are considered in the numerical examples. The derivation of this type of boundary conditions is based on the assumption for the microdeformation gradient in a form dependent on the macrodeformation gradient $\overline{\mathbf{F}}$ and microfluctuations $\tilde{\mathbf{w}}$

$$\mathbf{x} = \overline{\mathbf{F}} \cdot \mathbf{X} + \tilde{\mathbf{w}}. \tag{7}$$

The implementation of (7) in (6) leads to the conclusion that the microfluctuations $\tilde{\mathbf{w}}$ have to be periodic and the tractions $\mathbf{T}$ antiperiodic on the periodic boundary of the RVE:

$$\tilde{\mathbf{w}}^+ = \tilde{\mathbf{w}}^- \quad \text{and} \quad \mathbf{T}^+ = -\mathbf{T}^- \quad \text{on } \partial\mathcal{B}. \tag{8}$$

This closes the definition of the BVP at the microlevel which is now solved in terms of microfluctuations $\tilde{\mathbf{w}}$. The latter is used for the calculation of the stresses $\mathbf{P}$ at the microlevel and finally of the effective stresses according to the definition

$$\overline{\mathbf{P}} = \int_V \mathbf{P} dV. \tag{9}$$

Apart from the straightforward numerical application, the following special features of the explained concept are advantageous: The method is adapted for application in the case of finite deformation and applicable in the limiting case where the dimensions of the RVE are much smaller than the dimensions of the macroscopic body.

3. Mechanical model for viscoelastic curing of polymers

Viscous effects are the first new aspect of curing polymers considered in this paper. In order to give an appropriate mechanical model including this phenomenon, the generalized Maxwell model is considered (Fig. 1).

Here, a spring S is connected in parallel with the Maxwell body consisting of a dashpot D_1 and an additional spring S_1. Accordingly, the deformation of the second branch is decomposed into an elastic and a viscous part while the total energy includes two constituents, each depending on the elastic energy of one spring. These energy constituents are denoted as the equilibrium part

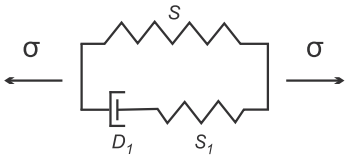

Fig. 1. Generalized Maxwell model.

Φ_{eq}, corresponding to the spring S, and as non-equilibrium part Φ_{neq} corresponding to the spring S_1

$$\Phi = \Phi_{\text{eq}} + \Phi_{\text{neq}}. \tag{10}$$

The chosen notation is straightforward since the deformations of the spring S_1 are time evolving even if the material parameter and the prescribed load are held constant. An additional decomposition into a volumetric and a deviatoric part is introduced for the purpose of modeling polymers with incompressible material behavior

$$\Phi_{\text{eq}}(\mathbf{u}, \theta, p) = \Phi_{\text{eq,dev}}\{\Psi_{\text{eq,dev}}(\mathbf{C}_{\text{iso}})\} + \Phi_{\text{eq,vol}}\{\Psi_{\text{eq,vol}}(\theta)\} + p[J(\mathbf{u}) - \theta], \tag{11}$$

$$\Phi_{\text{neq}}(\mathbf{u}, \theta_{\text{e}}, p_{\text{e}}) = \Phi_{\text{neq,dev}}(\mathbf{C}_{\text{e,iso}}) + \Phi_{\text{neq,vol}}(\theta_{\text{e}}) + p_{\text{e}}[J_{\text{e}}(\mathbf{u}) - \theta_{\text{e}}]. \tag{12}$$

Here, expression (11) coincides with the (1) such that the formulation (2) and (3) can be taken over for the definition of the equilibrium part of the energy density.

Unlike (11), the non-equilibrium part (12) is a new contribution. In this case, the material parameters are not necessarily time-dependent since the curing effects related to the spring in the Maxwell element (Fig. 1) can indirectly be controlled through the time-dependence of the relaxation time typical of the dashpot. Since the material parameters are constant in time, the non-equilibrium energy part does not need to be expressed in the form of a convolution integral. It can rather be equalized with the strain energy density

$$\Phi_{\text{neq}} = \Psi_{\text{neq}}. \tag{13}$$

Expression (12) only depends on the elastic deformations which are defined by the multiplicative decomposition of the total deformation gradient $\mathbf{F}$ into an elastic $\mathbf{F}_{\text{e}}$ and a viscous part $\mathbf{F}_{\text{i}}$

$$\mathbf{F} = \mathbf{F}_{\text{e}} \cdot \mathbf{F}_{\text{i}}. \tag{14}$$

Now, the further deformation quantities, namely the elastic, elastic isochoric and the inelastic part of the right Cauchy–Green deformation tensor, are expressed by using the standard definitions

$$\mathbf{C}_{\text{e}} = \mathbf{F}_{\text{i}}^{-\text{T}} \cdot \mathbf{C} \cdot \mathbf{F}_{\text{i}}^{-1}, \tag{15}$$

$$\mathbf{C}_{\text{e,iso}} = J_{\text{e}}^{-\frac{2}{3}} \mathbf{C}_{\text{e}}, \tag{16}$$

$$\mathbf{C}_{\text{i}} = \mathbf{F}_{\text{i}}^{\text{T}} \cdot \mathbf{F}_{\text{i}}. \tag{17}$$

As a further step, the proposed model is checked for thermodynamical consistency. On the assumption that the thermal influences are neglected, this condition requires that the internal power is higher than the rate of free energy density

$$\frac{1}{2}\mathbf{S} : \dot{\mathbf{C}} - \dot{\Phi} \geqslant 0. \tag{18}$$

After inserting Eqs. (11), (12), (2), (3) and (13) in (18), this inequality turns into the expression

$$\begin{aligned}
&\left[\mathbf{S} - \left[2\int_0^t \left[\mathbb{C}'_{\text{dev}}(\tau) : [\mathbf{C}_{\text{iso}}(t) - \mathbf{C}_{\text{iso}}(\tau)]\right] d\tau + 2p\frac{\partial J}{\partial \mathbf{C}}\right]\right.\\
&\quad \left. -2\mathbf{F}_{\text{i}}^{-1} \cdot \left[\frac{\partial \Phi_{\text{neq,dev}}(\mathbf{C}_{\text{e,iso}})}{\partial \mathbf{C}_{\text{e}}} + p_{\text{e}}\frac{\partial J_{\text{e}}}{\partial \mathbf{C}_{\text{e}}}\right] \cdot \mathbf{F}_{\text{i}}^{-\text{T}}\right] : \frac{1}{2}\dot{\mathbf{C}}\\
&\quad - \left[\int_0^t K'(\tau)[\theta(t) - \theta(\tau)] d\tau - p\right]\dot{\theta} - \left[\frac{\partial \Phi_{\text{neq,vol}}(\theta_{\text{e}})}{\partial \theta_{\text{e}}} - p_{\text{e}}\right]\dot{\theta}_{\text{e}}\\
&\quad - [J - \theta]\dot{p} - [J_{\text{e}} - \theta_{\text{e}}]\dot{p}_{\text{e}} - \frac{\partial \Phi_{\text{neq,dev}}(\mathbf{C}_{\text{e,iso}})}{\partial \mathbf{C}_{\text{e}}} : \frac{\partial \mathbf{C}_{\text{e}}}{\partial \mathbf{F}_{\text{i}}} : \dot{\mathbf{F}}_{\text{i}} \geqslant 0,
\end{aligned} \tag{19}$$

where the orthogonality between the deviatoric and volumetric quantities has been used in the transformation of the first term. Moreover, the terms depending on the rate of the same quantities are grouped together which is a form suitable for defining the

constitutive laws. For example, the second Piola–Kirchhoff stress tensor is obtained by setting the first term to zero

$$\mathbf{S} = 2\int_0^t \left[\mathbb{C}'_{\mathrm{dev}}(\tau) : [\mathbf{C}_{\mathrm{iso}}(t) - \mathbf{C}_{\mathrm{iso}}(\tau)]\right] d\tau + 2p\frac{\partial J}{\partial \mathbf{C}} + 2\mathbf{F}_{\mathrm{i}}^{-1} \cdot \left[\frac{\partial \Phi_{\mathrm{neq,dev}}(\mathbf{C}_{\mathrm{e,iso}})}{\partial \mathbf{C}_{\mathrm{e}}} + p_{\mathrm{e}}\frac{\partial J_{\mathrm{e}}}{\partial \mathbf{C}_{\mathrm{e}}}\right] \cdot \mathbf{F}_{\mathrm{i}}^{-\mathrm{T}}. \tag{20}$$

This quantity is then split into an equilibrium and a non-equilibrium part and further into a volumetric and a deviatoric part

$$\mathbf{S}_{\mathrm{eq,dev}} = 2\int_0^t \left[\mathbb{C}'_{\mathrm{dev}}(\tau) : [\mathbf{C}_{\mathrm{iso}}(t) - \mathbf{C}_{\mathrm{iso}}(\tau)]\right] d\tau, \tag{21}$$

$$\mathbf{S}_{\mathrm{eq,vol}} = 2p\frac{\partial J}{\partial \mathbf{C}} = pJ\mathbf{C}^{-1}, \tag{22}$$

$$\mathbf{S}_{\mathrm{neq,dev}} = 2\mathbf{F}_{\mathrm{i}}^{-1} \cdot \frac{\partial \Phi_{\mathrm{neq,dev}}(\mathbf{C}_{\mathrm{e,iso}})}{\partial \mathbf{C}_{\mathrm{e}}} \cdot \mathbf{F}_{\mathrm{i}}^{-\mathrm{T}}, \tag{23}$$

$$\mathbf{S}_{\mathrm{neq,vol}} = 2p_{\mathrm{e}}\mathbf{F}_{\mathrm{i}}^{-1} \cdot \frac{\partial J_{\mathrm{e}}}{\partial \mathbf{C}_{\mathrm{e}}} \cdot \mathbf{F}_{\mathrm{i}}^{-\mathrm{T}} = p_{\mathrm{e}}J_{\mathrm{e}}\mathbf{C}^{-1}. \tag{24}$$

In a similar manner, the relations for the hydrostatic pressure and the volume change are derived from (19)

$$p = \int_0^t K'(\tau)[\theta(t) - \theta(\tau)]d\tau, \tag{25}$$

$$\theta = J, \tag{26}$$

$$p_{\mathrm{e}} = \frac{\partial \Phi_{\mathrm{neq,vol}}(\theta_{\mathrm{e}})}{\partial \theta_{\mathrm{e}}}, \tag{27}$$

$$\theta_{\mathrm{e}} = J_{\mathrm{e}}. \tag{28}$$

It should be emphasized that Eqs. (26) and (28) are not real constitutive laws but the constraints introduced as the Lagrange terms in Eqs. (11) and (12). Moreover, the incremental formulations of expressions (21), (22) and (25) are more advantageous from the point of view of numerical implementation (Klinge, 2012)

$$\mathbf{S}_{\mathrm{eq,dev}}^{n+1} = \mathbf{S}_{\mathrm{eq,dev}}^{n} + 2\mathbb{C}_{\mathrm{dev}}^{n+1} : \left[\mathbf{C}_{\mathrm{iso}}^{n+1} - \mathbf{C}_{\mathrm{iso}}^{n}\right], \tag{29}$$

$$\mathbf{S}_{\mathrm{eq,vol}}^{n+1} = 2p^{n+1}\frac{\partial J^{n+1}}{\partial \mathbf{C}^{n+1}} = p^{n+1}J^{n+1}\left(\mathbf{C}^{-1}\right)^{n+1}, \tag{30}$$

$$p^{n+1} = p^n + K\left[\theta^{n+1} - \theta^n\right]. \tag{31}$$

After setting the definitions (20)–(28), inequality (19) yields still one last condition

$$-\frac{\partial \Phi_{\mathrm{neq,dev}}(\mathbf{C}_{\mathrm{e,iso}})}{\partial \mathbf{C}_{\mathrm{e}}} : \frac{\partial \mathbf{C}_{\mathrm{e}}}{\partial \mathbf{F}_{\mathrm{i}}} : \dot{\mathbf{F}}_{\mathrm{i}} \geqslant 0. \tag{32}$$

This inequality is commonly used for formulating thermodynamically consistent evolution equations for internal variables, but since this is not the object of the present contribution, the solution proposed by Reese and Govindjee (1998) is used for the necessary derivations and numerical examples. According to this proposal, the rate of the inelastic right Cauchy–Green deformation tensor is inversely proportional to the difference of the total and inelastic right Cauchy–Green deformation tensor, and the viscous behavior is characterized through the relaxation time T

$$\dot{\mathbf{C}}_{\mathrm{i}} = \frac{1}{T}[\mathbf{C} - \mathbf{C}_{\mathrm{i}}]. \tag{33}$$

Within the current model, the material parameter T is time-dependent since the curing process influences the viscous properties. The rate-dependent form of the inelastic Cauchy–Green strain tensor (33) is furthermore integrated by using the implicit Euler backward scheme in order to express the current value $\mathbf{C}_{\mathrm{i}}^{n+1}$

$$\mathbf{C}_{\mathrm{i}}^{n+1} = \omega^{n+1}\mathbf{C}^{n+1} + \frac{T^{n+1}}{\Delta t + T^{n+1}}\mathbf{C}_{\mathrm{i}}^{n}, \quad \omega^{n+1} = \frac{\Delta t}{\Delta t + T^{n+1}}. \tag{34}$$

Similarly as in case of quantities (29)–(31), this formulation is preferable from the point of view of the numerical implementation.

The derivation of an alternative proposal for evolution equation (33) is explained in A. It is based on the principles presented in the work of Reese and Govindjee (1998), and the obtained solution is a nonlinear evolution equation consistent with the particular choice for the strain energy considered in Section 5.

4. Mixed variational setting

For the sake of deriving the FEM model, the following multifield functional is considered

$$\Pi(\mathbf{u}, \theta, \theta_{\mathrm{e}}, p, p_{\mathrm{e}}) = \int_V \left[\Phi_{\mathrm{eq}}(\mathbf{u}, \theta, p) + \Phi_{\mathrm{neq}}(\mathbf{u}, \theta_{\mathrm{e}}, p_{\mathrm{e}})\right] dV + \Pi^{\mathrm{ext}}(\mathbf{u}), \tag{35}$$

where the first term on the right hand side represents the internal energy while $\Pi^{\mathrm{ext}}(\mathbf{u})$ is the potential of external forces. Since the finite deformations are considered, the minimization procedure in this case consists of two steps: the first variation of (35) is linearized in order to obtain the condition for the displacement increment $\Delta\mathbf{u}$:

$$\begin{aligned}
&\int_V \mathrm{Grad}\delta\mathbf{u} : \left[\mathrm{Grad}\Delta\mathbf{u} \cdot \left[\mathbf{S}_{\mathrm{eq}} + \mathbf{S}_{\mathrm{neq}}\right]\right] dV + \int_V \left[\mathrm{Grad}^{\mathrm{T}}\delta\mathbf{u} \cdot \mathbf{F}\right] \\
&: \left[\mathbb{E}_{\mathrm{eq}} + \mathbb{E}_{\mathrm{neq}}\right] : \left[\mathbf{F}^{\mathrm{T}} \cdot \mathrm{Grad}\Delta\mathbf{u}\right] dV \\
&+ \int_V \left[\left[\mathrm{Grad}^{\mathrm{T}}\delta\mathbf{u} \cdot \mathbf{F}\right] : J\mathbf{C}^{-1}\frac{1}{V}\frac{\partial^2 \Psi_{\mathrm{eq,vol}}}{\partial \theta^2}\int_V J\mathbf{C}^{-1} : \left[\mathbf{F}^{\mathrm{T}} \cdot \mathrm{Grad}\Delta\mathbf{u}\right] dV\right] dV \\
&+ \int_V \left[\left[\mathrm{Grad}^{\mathrm{T}}\delta\mathbf{u} \cdot \mathbf{F}\right] : J_{\mathrm{e}}\mathbf{C}^{-1}\frac{1}{V}\frac{\partial^2 \Psi_{\mathrm{neq,vol}}}{\partial \theta_{\mathrm{e}}^2}\int_V 2\frac{\partial J_{\mathrm{e}}}{\partial \mathbf{C}} : \left[\mathbf{F}^{\mathrm{T}} \cdot \mathrm{Grad}\Delta\mathbf{u}\right] dV\right] dV \\
&+ \Delta\delta_u\Pi^{\mathrm{ext}} = -\delta_u\Pi^{\mathrm{res}}.
\end{aligned} \tag{36}$$

Here, the residual is calculated as the first variation of the potential (35) with respect to the deformations

$$\delta_u\Pi^{\mathrm{res}} = \int_V \left[\mathrm{Grad}^{\mathrm{T}}\delta\mathbf{u} \cdot \mathbf{F}\right] : \left[\mathbf{S}_{\mathrm{eq}} + \mathbf{S}_{\mathrm{neq}}\right] dV + \delta_u\Pi^{\mathrm{ext}} \tag{37}$$

and the increment $\Delta\delta_u\Pi^{\mathrm{ext}}$ commonly vanishes since conservative loads are considered. The symbols $\mathbb{E}_{\mathrm{eq}}$ and $\mathbb{E}_{\mathrm{neq}}$ denote the equilibrium and the non-equilibrium material tangents

$$\mathbb{E}_{\mathrm{eq}} = 2\frac{\partial \mathbf{S}_{\mathrm{eq}}}{\partial \mathbf{C}}, \qquad \mathbb{E}_{\mathrm{neq}} = 2\frac{\partial \mathbf{S}_{\mathrm{neq}}}{\partial \mathbf{C}}, \tag{38}$$

which are furthermore decomposed into a deviatoric and a volumetric part

$$\mathbb{E}_{\mathrm{eq,dev}}^{n+1} = 2\frac{\partial \mathbf{S}_{\mathrm{eq,dev}}^{n+1}}{\partial \mathbf{C}^{n+1}} = 4\mathbb{C}_{\mathrm{dev}}^{n+1} : \frac{\partial \mathbf{C}_{\mathrm{iso}}^{n+1}}{\partial \mathbf{C}^{n+1}} + 4\left[\mathbf{C}_{\mathrm{iso}}^{n+1} - \mathbf{C}_{\mathrm{iso}}^{n}\right] : \mathfrak{U}_{\mathrm{dev}}^{n+1}, \tag{39}$$

$$\mathbb{E}_{\mathrm{eq,vol}}^{n+1} = 2\frac{\partial \mathbf{S}_{\mathrm{eq,dev}}^{n+1}}{\partial \mathbf{C}^{n+1}} = 4p^{n+1}\left[\frac{\partial^2 J}{\partial \mathbf{C}^2}\right]^{n+1}, \tag{40}$$

$$\mathbb{E}_{\mathrm{neq,dev}} = 2\frac{\partial \mathbf{S}_{\mathrm{neq,dev}}}{\partial \mathbf{C}}, \tag{41}$$

$$\mathbb{E}_{\mathrm{neq,vol}} = 2\frac{\partial \mathbf{S}_{\mathrm{neq,vol}}}{\partial \mathbf{C}}. \tag{42}$$

Symbol $\mathfrak{U}_{\mathrm{dev}}$ in (39) denotes the following sixth order tensor

$$\mathfrak{U}_{\mathrm{dev}}^{n+1} = \frac{\partial \mathbb{C}_{\mathrm{dev}}^{n+1}}{\partial \mathbf{C}^{n+1}}. \tag{43}$$

5. Viscoelastic neo-Hooke-type curing material

The application of the model developed will be demonstrated by way of an example in which a neo-Hooke-type strain energy is assumed as a basis for the definition of both parts of the free energy density

$$\Psi_{\mathrm{eq}}(\mathbf{u},\theta,p,t)=\frac{\mu(t)}{2}\left[\mathbf{C}_{\mathrm{iso}}:\mathbf{I}-3\right]+\kappa(t)[\theta\ln\theta-\theta+1]+p[J-\theta], \tag{44}$$

$$\Psi_{\mathrm{neq}}(\mathbf{u},\theta_{\mathrm{e}},p_{\mathrm{e}})=\frac{\mu_{\mathrm{e}}}{2}\left[\mathbf{C}_{\mathrm{e,iso}}:\mathbf{I}-3\right]+\kappa_{\mathrm{e}}[\theta_{\mathrm{e}}\ln\theta_{\mathrm{e}}-\theta_{\mathrm{e}}+1]+p_{\mathrm{e}}[J_{\mathrm{e}}-\theta_{\mathrm{e}}]. \tag{45}$$

In each of these equations, the first term represents the deviatoric energy density, the second term is the volumetric energy density and the last term is the Lagrange term coupling the volumetric change θ with the deformations $\mathbf{u}$. Symbols$\kappa(t)$ and κ_{e} denote the bulk moduli and$\mu(t)$ and μ_{e} the shear moduli. The variable t in Eq. (44) is introduced to emphasize the difference between the time-dependent and time-independent material constants.

As mentioned in Section 3, the equilibrium energy part depends on the total deformations and on the time-dependent material parameters ($\kappa=\kappa(t)$ and $\mu=\mu(t)$) while the non-equilibrium part depends on the elastic deformations and material parameters being constant in time (κ_{e} and μ_{e}). The evolution of the elastic deformations is indirectly controlled through the evolution of the inelastic material parameter, namely the relaxation time.

5.1. Deviatoric quantities

The overview of the main relations necessary for an FEM implementation starts with the equilibrium isochoric quantities. The second Piola–Kirchhoff stress tensor, the material tangent and the necessary derivatives in this case have the following form (see Eqs. (29), (39), (4) and (43))

$$\mathbf{S}^{n+1}_{\mathrm{eq,dev}}=\mathbf{S}^{n}_{\mathrm{dev}}+2\mathbb{C}^{n+1}_{\mathrm{dev}}:\left[\mathbf{C}^{n+1}_{\mathrm{iso}}-\mathbf{C}^{n}_{\mathrm{iso}}\right], \tag{46}$$

$$\mathbb{E}^{n+1}_{\mathrm{eq,dev}}=4\mathbb{C}^{n+1}_{\mathrm{dev}}:\frac{\partial\mathbf{C}^{n+1}_{\mathrm{iso}}}{\partial\mathbf{C}^{n+1}}+4\left[\mathbf{C}^{n+1}_{\mathrm{iso}}-\mathbf{C}^{n}_{\mathrm{iso}}\right]:\mathfrak{U}^{n+1}_{\mathrm{dev}}, \tag{47}$$

$$\mathbb{C}_{\mathrm{dev}}=4\frac{\partial^2\Psi_{\mathrm{eq,dev}}}{\partial\mathbf{C}^2}, \tag{48}$$

$$\mathfrak{U}_{\mathrm{dev}}=\frac{\partial\mathbb{C}_{\mathrm{dev}}}{\partial\mathbf{C}}. \tag{49}$$

For assumption (44), the last two equations transform into expressions

$$\begin{aligned}\left(\mathbb{C}_{\mathrm{eq,dev}}\right)_{klmn}=&-\frac{2}{3}\mu J^{-\frac{2}{3}}I_{ij}\left[\left[(\mathbb{I})_{ijkl}\left(\mathbf{C}^{-1}\right)_{mn}-\frac{1}{3}C_{ij}(\mathbb{B})_{klmn}\right]\right.\\&\left.+\left[(\mathbb{I})_{ijmn}\left(\mathbf{C}^{-1}\right)_{kl}+C_{ij}(\mathbb{A})_{klmn}\right]\right],\end{aligned} \tag{50}$$

$$\begin{aligned}\left(\mathfrak{U}_{\mathrm{eq,dev}}\right)_{klmnop}=&\frac{2}{3}\mu J^{-\frac{2}{3}}I_{ij}\left[\frac{1}{3}\left[(\mathbb{I})_{ijkl}-\frac{1}{3}C_{ij}\left(\mathbf{C}^{-1}\right)_{kl}\right](\mathbb{B})_{mnop}\right.\\&+\frac{1}{3}\left[(\mathbb{I})_{ijmn}(\mathbb{B})_{klop}+C_{ij}(\mathbb{A})_{klmn}\left(\mathbf{C}^{-1}\right)_{op}\right]\\&+\frac{1}{3}\left[(\mathbb{I})_{ijop}(\mathbb{B})_{klmn}+C_{ij}(\mathbb{A})_{klop}\left(\mathbf{C}^{-1}\right)_{mn}\right]\\&-\left[(\mathbb{I})_{ijkl}-\frac{1}{3}C_{ij}\left(\mathbf{C}^{-1}\right)_{kl}\right](\mathbb{A})_{mnop}\\&\left.-\left[(\mathbb{I})_{ijmn}(\mathbb{A})_{klop}+(\mathbb{I})_{ijop}(\mathbb{A})_{klmn}+C_{ij}(\mathfrak{D})_{klmnop}\right]\right],\end{aligned} \tag{51}$$

where the following notation is used (Klinge, 2012)

$$(\mathbb{A})_{ijkl}=\left(\frac{\partial\mathbf{C}^{-1}}{\partial\mathbf{C}}\right)_{ijkl}=-\frac{1}{2}\left[\left(\mathbf{C}^{-1}\right)_{ik}\left(\mathbf{C}^{-1}\right)_{jl}+\left(\mathbf{C}^{-1}\right)_{il}\left(\mathbf{C}^{-1}\right)_{jk}\right],$$

$$(\mathbb{B})_{ijkl}=\left(\mathbf{C}^{-1}\otimes\mathbf{C}^{-1}\right)_{ijkl}=\left(\mathbf{C}^{-1}\right)_{ij}\left(\mathbf{C}^{-1}\right)_{kl},$$

$$\begin{aligned}(\mathfrak{D})_{ijklmn}=&\left(\frac{\partial\mathbb{A}}{\partial\mathbf{C}}\right)_{ijklmn}\\=&-\frac{1}{2}\left[(\mathbb{A})_{ikmn}\left(\mathbf{C}^{-1}\right)_{jl}+\left(\mathbf{C}^{-1}\right)_{ik}(\mathbb{A})_{jlmn}+(\mathbb{A})_{ilmn}\left(\mathbf{C}^{-1}\right)_{jk}\right.\\&\left.+\left(\mathbf{C}^{-1}\right)_{il}(\mathbb{A})_{jkmn}\right].\end{aligned}$$

The non-equilibrium deviatoric second Piola–Kirchhoff stress tensor and material tangent are defined by Eqs. (23) and (41)

$$\mathbf{S}_{\mathrm{neq,dev}}=2\mathbf{F}_{\mathrm{i}}^{-1}\cdot\frac{\partial\Phi_{\mathrm{neq,dev}}}{\partial\mathbf{C}_{\mathrm{e}}}\cdot\mathbf{F}_{\mathrm{i}}^{-\mathrm{T}}, \tag{52}$$

$$\mathbb{E}_{\mathrm{neq,dev}}=2\frac{\partial\mathbf{S}_{\mathrm{neq,dev}}}{\partial\mathbf{C}}. \tag{53}$$

Their extended formulation is based on the assumption for the energy density (45) but also on the solution for the evolution of the inelastic deformations (34)

$$\left(\mathbf{S}_{\mathrm{neq,dev}}\right)_{ij}=\mu_{\mathrm{e}}J_{\mathrm{e}}^{-\frac{2}{3}}\left[\left(\mathbf{C}_{\mathrm{i}}^{-1}\right)_{ij}-\frac{1}{3}\mathrm{tr}\mathbf{C}_{\mathrm{e}}\left(\mathbf{C}^{-1}\right)_{ij}\right], \tag{54}$$

$$\begin{aligned}\left(\mathbb{E}_{\mathrm{neq,dev}}\right)_{ijkl}=&2\mu_{\mathrm{e}}\left[\left[\left(\mathbf{C}_{\mathrm{i}}^{-1}\right)_{ij}-\frac{1}{3}\mathrm{tr}C_{\mathrm{e}}\left(\mathbf{C}^{-1}\right)_{ij}\right]Q_{kl}\right.\\&\left.+J_{\mathrm{e}}^{-\frac{2}{3}}\left[\omega(\mathbb{D})_{ijkl}-\frac{1}{3}\left(\mathbf{C}^{-1}\right)_{ij}M_{kl}-\frac{1}{3}\mathrm{tr}\mathbf{C}_{\mathrm{e}}(\mathbb{A})_{ijkl}\right]\right].\end{aligned} \tag{55}$$

The following abbreviated notation applies to the previous equations

$$\mathbf{M}=\frac{\partial\mathrm{tr}\mathbf{C}_{\mathrm{e}}}{\partial\mathbf{C}}, \tag{56}$$

$$\mathbf{Q}=\frac{\partial J_{\mathrm{e}}^{-\frac{2}{3}}}{\partial\mathbf{C}}=-\frac{1}{3}J_{\mathrm{e}}^{-\frac{2}{3}}\left[\mathbf{C}^{-1}-\omega\mathbf{C}_{\mathrm{i}}^{-1}:\mathbb{I}\right], \tag{57}$$

$$(\mathbb{D})_{ijkl}=\left(\frac{\partial\mathbf{C}_{\mathrm{i}}^{-1}}{\partial\mathbf{C}_{\mathrm{i}}}\right)_{ijkl}=-\frac{1}{2}\left[\left(\mathbf{C}_{\mathrm{i}}^{-1}\right)_{ik}\left(\mathbf{C}_{\mathrm{i}}^{-1}\right)_{jl}+\left(\mathbf{C}_{\mathrm{i}}^{-1}\right)_{il}\left(\mathbf{C}_{\mathrm{i}}^{-1}\right)_{jk}\right], \tag{58}$$

where the fourth order tensor $\mathbf{M}$ (56) deserves special attention. According to the definition (16), the quantity $\mathbf{C}_{\mathrm{e}}$ and thus the tensor $\mathbf{M}$ are dependent on the inelastic deformation gradient $\mathbf{F}_{\mathrm{i}}$, which, however, cannot be determined uniquely since the evolution of inelastic deformations is controlled by the evolution of the right Cauchy–Green deformation tensor (33). One possible way to cope with this shortcoming is based on the use of the polar decomposition $\mathbf{F}_{\mathrm{i}}=\mathbf{R}_{\mathrm{i}}\cdot\mathbf{U}_{\mathrm{i}}$. According to this theorem, the decomposition of the deformation gradient into a rotation tensor $\mathbf{R}_{\mathrm{i}}$ and a right stretch tensor $\mathbf{U}_{\mathrm{i}}$ is unique. Moreover, the rotation $\mathbf{R}_{\mathrm{i}}$ is the rigid body motion and does not have any influence on the deformation energy. This implies that the original elastic right Cauchy–Green deformation tensor $\mathbf{C}_{\mathrm{e}}$ in Eq. (56) can be replaced by a new quantity $\mathbf{C}_{\mathrm{e}}^{\mathrm{u}}$ depending on the stretch tensor $\mathbf{U}_{\mathrm{i}}$ instead of on the deformation gradient $\mathbf{F}_{\mathrm{i}}$

$$\mathbf{C}_{\mathrm{e}}=\mathbf{F}_{\mathrm{i}}^{-\mathrm{T}}\cdot\mathbf{C}\cdot\mathbf{F}_{\mathrm{i}}^{-1}\quad\rightarrow\quad\mathbf{C}_{\mathrm{e}}^{\mathrm{u}}=\mathbf{U}_{\mathrm{i}}^{-1}\cdot\mathbf{C}\cdot\mathbf{U}_{\mathrm{i}}^{-1}. \tag{59}$$

In an analogous way, the derivative $\frac{\partial\mathrm{tr}\mathbf{C}_{\mathrm{e}}}{\partial\mathbf{C}}$ is replaced by its counterpart $\frac{\partial\mathrm{tr}\mathbf{C}_{\mathrm{e}}^{\mathrm{u}}}{\partial\mathbf{C}}$ which is calculated numerically

$$\left(\frac{\partial \mathrm{tr}\mathbf{C}_{\mathrm{e}}^{\mathrm{u}}}{\partial \mathbf{C}}\right) \approx \frac{1}{\epsilon}\left[\mathbf{I} : \left[\left(\mathbf{U}_{\epsilon\mathrm{i}}^{ij}\right)^{-1} \cdot \mathbf{C}_{\epsilon}^{ij} \cdot \left(\mathbf{U}_{\epsilon\mathrm{i}}^{ij}\right)^{-1}\right] - \mathbf{I} : \left[\mathbf{U}_{\mathrm{i}}^{-1} \cdot \mathbf{C} \cdot \mathbf{U}_{\mathrm{i}}^{-1}\right]\right]. \tag{60}$$

Here, $\mathbf{C}_{\epsilon}^{ij}$ denotes the perturbed right Cauchy–Green deformation tensor defined as $\mathbf{C}_{\epsilon}^{ij} = \mathbf{C} + \epsilon \mathbf{e}_i \otimes \mathbf{e}_j$, symbol $\epsilon \ll 1$ denotes a small perturbation, $e_i, i = 1, 2, 3$ are the basis vectors and $\mathbf{U}_{\epsilon\mathrm{i}}^{ij}$ is the inelastic right stretch tensor corresponding to $\mathbf{C}_{\epsilon}^{ij}$.

Apart from the previous procedure, another way to overcome the difficulties related to the calculation of the derivative (56) is to assume an alternative evolution equation in the place of (33). Such a law is derived and explained in A, however, its numerical implementation is an issue which will be studied in some of the future works.

5.2. Volumetric quantities

The summary of the volumetric quantities starts with the equilibrium part (Eqs. (31), (5), (22) and (40))

$$p^{n+1} = p^n + K^{n+1}\left[\theta^{n+1} - \theta^n\right], \quad K = \frac{\partial^2 \Psi_{\mathrm{vol}}(\theta)}{\partial \theta^2}, \tag{61}$$

$$\mathbf{S}_{\mathrm{eq,vol}} = pJ\mathbf{C}^{-1}, \tag{62}$$

$$\mathbb{E}_{\mathrm{eq,vol}} = 2\frac{\partial \mathbf{S}_{\mathrm{eq,vol}}}{\partial \mathbf{C}} = pJ[\mathbb{B} + 2\mathbb{A}]. \tag{63}$$

Here, only the hydrostatic pressure directly depends on the choice of the strain energy density (44)

$$p^{n+1} = p^n + \left[\frac{\kappa}{\theta}\right]^{n+1}\left[\theta^{n+1} - \theta^n\right], \tag{64}$$

while the remaining two quantities depend on the hydrostatic pressure and thus indirectly on the assumption (44).

The same situation occurs in case of the non-equilibrium quantities. According to the definition (27) and assumption (45), the elastic hydrostatic pressure has the following form

$$p_{\mathrm{e}} = \frac{\partial \Phi_{\mathrm{neq,vol}}}{\partial \theta_{\mathrm{e}}} = \kappa_{\mathrm{e}} \ln \theta_{\mathrm{e}}, \tag{65}$$

which is now used in the calculation of the stresses and the material tangent (Eqs. (24) and (42))

$$\mathbf{S}_{\mathrm{neq,vol}} = p_{\mathrm{e}} J_{\mathrm{e}} \mathbf{C}^{-1}, \tag{66}$$

$$\mathbb{E}_{\mathrm{neq,vol}} = 2\frac{\partial \mathbf{S}_{\mathrm{neq,vol}}}{\partial \mathbf{C}} = 2p_{\mathrm{e}}\left[\mathbf{C}^{-1} \otimes \frac{\partial J_{\mathrm{e}}}{\partial \mathbf{C}} + J_{\mathrm{e}}\mathbb{A}\right], \tag{67}$$

$$\frac{\partial J_{\mathrm{e}}}{\partial \mathbf{C}} = \frac{\partial (J J_{\mathrm{i}}^{-1})}{\partial \mathbf{C}} = \frac{1}{2} J_{\mathrm{e}}\left[\mathbf{C}^{-1} - \omega \mathbf{C}_{\mathrm{i}}^{-1} : \mathbb{I}\right]. \tag{68}$$

Please note that all definitions in Section 5 are related to the current time step $n+1$. However, this is explicitly written only in equations depending on the values from the different time steps. If an expression only depends on the quantities related to the same time step, this notation is omitted.

6. Modeling of curing shrinkage

In addition to the viscous effects, this paper also deals with the modeling of the volume shrinkage. This effect is a result of chemical reactions, binding forces and decreasing mean distances between the polymer molecules. Additionally, a high hydrostatic compression or tension can also counteract or enhance this effect. However, the last influence is negligible under stress magnitudes which occur during technical polymer curing such that shrinkage in this context can be considered as an autogeneous process. For its modeling, a multiplicative decomposition of the deformation gradient into a mechanical part $\mathbf{F}_{\mathrm{m}}$ and a shrinkage part $\mathbf{F}_{\mathrm{s}}$, is assumed

$$\mathbf{F} = \mathbf{F}_{\mathrm{m}} \cdot \mathbf{F}_{\mathrm{s}}. \tag{69}$$

In this proposal, the mechanical part coincides with the deformation gradient typical of the viscoelastic curing (Eq. (14))

$$\mathbf{F}_{\mathrm{m}} = \mathbf{F}_{\mathrm{e}} \cdot \mathbf{F}_{\mathrm{i}}, \tag{70}$$

while the shrinkage deformation gradient is assumed in the form proposed by Lion and Höfer (2007)

$$\mathbf{F}_{\mathrm{s}} = [1 + \alpha s]^{\frac{1}{3}}\mathbf{I}, \tag{71}$$

where $s \leqslant 0$ denotes the magnitude of the shrinking volume and the degree of cure $\alpha \in [0, 1]$ is a time-dependent parameter controlling the influence of curing on the shrinkage. Solution (71) enables the right Cauchy–Green strain tensor to be expressed as a linear function in its mechanical counterpart

$$\mathbf{C} = \mathbf{F}_{\mathrm{s}}^{\mathrm{T}} \cdot \mathbf{C}_{\mathrm{m}} \cdot \mathbf{F}_{\mathrm{s}} = [1 + \alpha s]^{\frac{2}{3}}\mathbf{C}_{\mathrm{m}}. \tag{72}$$

Apart from the new definition for the deformation gradient, the thermodynamical description of the viscoelastic curing including shrinkage does nor require any new assumptions. The expressions for the free energy densities (Eqs. (11) and (12)) remain valid here, but they are now written in terms of the mechanical quantities $\Phi = \Phi_{\mathrm{m}}(\mathbf{u}, \theta_{\mathrm{m}}, p_{\mathrm{m}})$. The check of the thermodynamical consistency (18) yields the following relationships

$$\mathbf{S} = 2\mathbf{F}_{\mathrm{s}}^{-1} \cdot \left[\frac{\partial \Phi_{\mathrm{m,dev}}(\mathbf{u})}{\partial \mathbf{C}_{\mathrm{m}}} + p_{\mathrm{m}}\frac{\partial J_{\mathrm{m}}}{\partial \mathbf{C}_{\mathrm{m}}}\right] \cdot \mathbf{F}_{\mathrm{s}}^{-\mathrm{T}}, \tag{73}$$

$$p_{\mathrm{m}} = \frac{\partial \Phi_{\mathrm{m,vol}}(\theta_{\mathrm{m}})}{\partial \theta_{\mathrm{m}}}, \tag{74}$$

$$\theta_{\mathrm{m}} = J_{\mathrm{m}}, \tag{75}$$

where the second Piola–Kirchhoff stress tensor can be decomposed into a deviatoric and a volumetric part

$$\mathbf{S}_{\mathrm{dev}} = 2\mathbf{F}_{\mathrm{s}}^{-1} \cdot \left[\frac{\partial \Phi_{\mathrm{m,dev}}(\mathbf{u})}{\partial \mathbf{C}_{\mathrm{m}}}\right] \cdot \mathbf{F}_{\mathrm{s}}^{-\mathrm{T}} = [1 + \alpha s]^{-\frac{2}{3}}\mathbf{S}_{\mathrm{m,dev}}, \tag{76}$$

$$\mathbf{S}_{\mathrm{vol}} = 2\mathbf{F}_{\mathrm{s}}^{-1} \cdot \left[p_{\mathrm{m}}\frac{\partial J_{\mathrm{m}}}{\partial \mathbf{C}_{\mathrm{m}}}\right] \cdot \mathbf{F}_{\mathrm{s}}^{-\mathrm{T}} = [1 + \alpha s]^{-\frac{2}{3}}\mathbf{S}_{\mathrm{m,vol}}. \tag{77}$$

Correspondingly, the material tangents can be expressed as follows

$$\mathbb{E}_{\mathrm{dev}} = 2\frac{\partial \mathbf{S}_{\mathrm{dev}}}{\partial \mathbf{C}} = [1 + \alpha s]^{-\frac{4}{3}}\mathbb{E}_{\mathrm{m,dev}}, \tag{78}$$

$$\mathbb{E}_{\mathrm{vol}} = 2\frac{\partial \mathbf{S}_{\mathrm{vol}}}{\partial \mathbf{C}} = [1 + \alpha s]^{-\frac{4}{3}}\mathbb{E}_{\mathrm{m,vol}}. \tag{79}$$

Relation (69), also causes the second variation (36) to be written in a slightly different manner

$$\begin{aligned}
&\int_V \mathrm{Grad}\delta\mathbf{u} : \left[\mathrm{Grad}\Delta\mathbf{u} \cdot \left[[1 + \alpha s]^{-\frac{2}{3}}\left[\mathbf{S}_{\mathrm{m,dev}} + \mathbf{S}_{\mathrm{m,vol}}\right]\right]\right] dV \\
&+ \int_V \left[\mathrm{Grad}^{\mathrm{T}}\delta\mathbf{u} \cdot \mathbf{F}\right] : \left[[1 + \alpha s]^{-\frac{4}{3}}\left[\mathbb{E}_{\mathrm{m,dev}} + \mathbb{E}_{\mathrm{m,vol}}\right]\right] : \left[\mathbf{F}^{\mathrm{T}} \cdot \mathrm{Grad}\Delta\mathbf{u}\right] dV \\
&+ \int_V \left[\left[\mathrm{Grad}^{\mathrm{T}}\delta\mathbf{u} \cdot \mathbf{F}\right] : J_{\mathrm{m}}\mathbf{C}_{\mathrm{m}}^{-1}\left[\frac{1}{V}[1 + \alpha s]^{-\frac{4}{3}}\frac{\partial^2 \Psi_{\mathrm{eq,vol}}}{\partial \theta_{\mathrm{m}}^2}\right]\right. \\
&\times \left.\int_V J_{\mathrm{m}}\mathbf{C}_{\mathrm{m}}^{-1} : \left[\mathbf{F}^{\mathrm{T}} \cdot \mathrm{Grad}\Delta\mathbf{u}\right] dV\right] dV \\
&+ \int_V \left[\left[\mathrm{Grad}^{\mathrm{T}}\delta\mathbf{u} \cdot \mathbf{F}\right] : J_{\mathrm{e}}\mathbf{C}_{\mathrm{m}}^{-1}\left[\frac{1}{V}[1 + \alpha s]^{-\frac{4}{3}}\frac{\partial^2 \Psi_{\mathrm{neq,vol}}}{\partial \theta_{\mathrm{m}}^2}\right]\right. \\
&\times \left.\int_V 2\frac{J_{\mathrm{e}}}{\mathbf{C}_{\mathrm{m}}} : \left[\mathbf{F}^{\mathrm{T}} \cdot \mathrm{Grad}\Delta\mathbf{u}\right] dV\right] dV + \Delta\delta_u \Pi^{\mathrm{ext}} = -\delta_u \Pi^{\mathrm{res}}.
\end{aligned} \tag{80}$$

This is an expression more general than (36), and special cases such as the elastic or viscoelastic curing can be easily deduced from it by zeroing the corresponding terms.

Please recall that all mechanical quantities appearing in this section coincide with the quantities related to the viscoelastic curing as defined in Sections 3 and 4.

7. Multiscale approach for microheterogeneous curing materials

For the simulation of microheterogeneous materials, the concept recapitulated in Section 2.2 is used. Its implementation is demonstrated on the basis of examples in which the RVE consists of a curing polymer combined with purely elastic material. To this end, the finite element type corresponding to the nonlinear elastic behavior is considered at the macrolevel. This choice is substantiated by the fact that the curing and the shrinkage affect the calculation of the microscopic stresses and thus automatically the effective stresses transferred to the macrolevel. An analogous concept can be applied for the alternative combinations of materials at the microlevel.

The nonlinear elastic behavior at the macrolevel is simulated on the basis of the following three-field potential

$$\overline{\Pi}(\bar{\mathbf{u}},\bar{\theta},\bar{p}) = \int_{\overline{V}} \left[\overline{\Psi}_{\mathrm{vol}}(\bar{\theta}) + \overline{\Psi}_{\mathrm{dev}}(\overline{\mathbf{C}}_{\mathrm{iso}}(\bar{\mathbf{u}})) + \bar{p}(\bar{J}(\bar{\mathbf{u}}) - \bar{\theta}) \right] d\overline{V} + \overline{\Pi}^{\mathrm{ext}}, \tag{81}$$

where the values belonging to the macrolevel are denoted by the overbar symbol and the effective strain energy density is decomposed into a volumetric and a deviatoric part since incompressible material behavior might occur at the macrolevel. The potential (81) and its second variation serve as the basis for the development of the so called Q1P0 element (Simo and Hughes, 1997):

$$\begin{aligned}
&\int_{\overline{V}} \overline{\mathrm{Grad}}\delta\bar{\mathbf{u}} : \left[\overline{\mathrm{Grad}}\Delta\bar{\mathbf{u}} \cdot \left[\overline{\mathbf{S}}_{\mathrm{dev}} + \overline{\mathbf{S}}_{\mathrm{vol}} \right] \right] d\overline{V} \\
&+ \int_{\overline{V}} \left[\overline{\mathrm{Grad}}^{\mathrm{T}}\delta\bar{\mathbf{u}} \cdot \overline{\mathbf{F}} \right] : \left[\overline{\mathbb{E}}_{\mathbf{dev}} + \overline{\mathbb{E}}_{\mathbf{vol}} \right] : \left[\overline{\mathbf{F}}^{\mathbf{T}} \cdot \overline{\mathbf{Grad}}\Delta\bar{\mathbf{u}} \right] d\overline{\mathbf{V}} \\
&+ \int_{\overline{\mathbf{V}}} \left[\left[\overline{\mathbf{Grad}}^{\mathbf{T}}\delta\bar{\mathbf{u}} \cdot \overline{\mathbf{F}} \right] : \overline{\mathbf{J}}\overline{\mathbf{C}}^{-\mathbf{1}} \left[\frac{\mathbf{1}}{\overline{\mathbf{V}}} \frac{\partial^{\mathbf{2}} \overline{\Psi}_{\mathbf{vol}}}{\partial \bar{\theta}^{\mathbf{2}}} \right] \int_{\overline{\mathbf{V}}} \overline{\mathbf{J}}\overline{\mathbf{C}}^{-\mathbf{1}} : \left[\overline{\mathbf{F}}^{\mathbf{T}} \cdot \overline{\mathbf{Grad}}\Delta\bar{\mathbf{u}} \right] d\overline{\mathbf{V}} \right] d\overline{\mathbf{V}} \\
&+ \Delta\delta_{\bar{\mathbf{u}}} \overline{\Pi}^{\mathbf{ext}} = -\delta_{\bar{\mathbf{u}}} \overline{\Pi}^{\mathbf{res}}(\bar{\mathbf{u}}),
\end{aligned} \tag{82}$$

$$\bar{\mathbf{u}} = \bar{\mathbf{u}}_{\mathbf{0}}, \quad \delta\bar{\mathbf{u}} = 0, \quad \Delta\bar{\mathbf{u}} = \mathbf{0} \quad \text{on } \partial\overline{\mathcal{B}}_{\sqcap}. \tag{83}$$

Here, Eq. (83) represents Dirichlet boundary conditions, symbol $\overline{\mathcal{B}}_{\sqcap}$ is used to denote the boundary part with the prescribed deformations $\bar{\mathbf{u}}_0$ and the residual $\delta_{\bar{u}}\overline{\Pi}^{\mathrm{res}}(\bar{\mathbf{u}})$ represents the current value of the first variation of the potential

$$\delta_{\bar{u}}\overline{\Pi}^{\mathrm{res}} = \int_{\overline{V}} \left[\overline{\mathrm{Grad}}^{\mathrm{T}}\delta\bar{\mathbf{u}} \cdot \overline{\mathbf{F}} \right] : \left[\overline{\mathbf{S}}_{\mathrm{dev}} + \overline{\mathbf{S}}_{\mathrm{dev}} \right] d\overline{V} + \delta_{\bar{u}}\overline{\Pi}^{\mathrm{ext}}. \tag{84}$$

The BVP (82) and (83) is formulated in terms of unknown displacements, however its direct solution is not possible since the effective strain energy densities $\overline{\Psi}_{\mathrm{dev}}$ and $\overline{\Psi}_{\mathrm{vol}}$ are not available. For their calculation and the calculation of their derivatives $\overline{\mathbf{S}}_{\mathbf{dev}}$, $\overline{\mathbf{S}}_{\mathbf{vol}}$, $\overline{\mathbb{E}}_{\mathbf{dev}}$, $\overline{\mathbb{E}}_{\mathbf{vol}}$, $\frac{\partial^{\mathbf{2}}\overline{\Psi}_{\mathbf{vol}}}{\partial\bar{\Theta}^{\mathbf{2}}}$, the results from the microscale are necessary. More precisely, the solution of the microscopic BVP yields data on the microfluctuations and thus on the microscopic and macroscopic stresses (Eq. (9)).

The heterogeneous RVE consists of two phases, i.e. two types of material. The first phase at the microlevel (index "1") is the viscoelastic curing material with the shrinkage. Its FEM implementation is based on the expression (80) which is here recalled in terms of microfluctuations $\tilde{\mathbf{w}}$ and the macroscopic deformation tensor $\overline{\mathbf{F}}$. The increment of the first variation of the internal energy $\Delta\delta\Pi_1$ and the current residual $\delta_{\tilde{\mathbf{w}}}\Pi_1^{\mathrm{res}}$ are written separately for the sake of a clear formulation of the complete microscopic BVP

$$\begin{aligned}
\Delta\delta\Pi_1 = &\int_{V_1} \mathrm{Grad}\delta\tilde{\mathbf{w}} : \left[\mathrm{Grad}\Delta\tilde{\mathbf{w}} \cdot \left[[1+\alpha s]^{-\frac{2}{3}} [\mathbf{S}_{\mathrm{m,dev}} + \mathbf{S}_{\mathrm{m,vol}}] \right] \right] dV \\
&+ \int_{V_1} \left[\mathrm{Grad}^{\mathrm{T}}\delta\tilde{\mathbf{w}} \cdot \mathbf{F} \right] : \left[[1+\alpha s]^{-\frac{4}{3}} [\mathbb{E}_{\mathrm{m,dev}} + \mathbb{E}_{\mathrm{m,vol}}] \right] : \left[\mathbf{F}^{\mathrm{T}} \cdot \mathrm{Grad}\Delta\tilde{\mathbf{w}} \right] dV \\
&+ \int_{V_1} \left[\left[\mathrm{Grad}^{\mathrm{T}}\delta\tilde{\mathbf{w}} \cdot \mathbf{F} \right] : J_{\mathrm{m}}\mathbf{C}_{\mathrm{m}}^{-1} \left[\frac{1}{V_1} [1+\alpha s]^{-\frac{4}{3}} \frac{\partial^2 \Psi_{\mathrm{eq,vol}}}{\partial\theta_{\mathrm{m}}^2} \right] \right. \\
&\times \left. \int_V J_{\mathrm{m}}\mathbf{C}_{\mathrm{m}}^{-1} : \left[\mathbf{F}^{\mathrm{T}} \cdot \mathrm{Grad}\Delta\tilde{\mathbf{w}} \right] dV \right] dV \\
&+ \int_{V_1} \left[\left[\mathrm{Grad}^{\mathrm{T}}\delta\tilde{\mathbf{w}} \cdot \mathbf{F} \right] : J_{\mathrm{e}}\mathbf{C}_{\mathrm{m}}^{-1} \left[\frac{1}{V_1} [1+\alpha s]^{-\frac{4}{3}} \frac{\partial^2 \Psi_{\mathrm{neq,vol}}}{\partial\theta_{\mathrm{m}}^2} \right] \right. \\
&\times \left. \int_V 2\frac{J_{\mathrm{e}}}{\mathbf{C}_{\mathrm{m}}} : \left[\mathbf{F}^{\mathrm{T}} \cdot \mathrm{Grad}\Delta\tilde{\mathbf{w}} \right] dV \right] dV,
\end{aligned} \tag{85}$$

$$\delta_{\tilde{\mathbf{w}}}\Pi_1^{\mathrm{res}}(\tilde{\mathbf{w}},\overline{\mathbf{F}}) = \int_{V_1} \left[\mathrm{Grad}^{\mathrm{T}}\delta\tilde{\mathbf{w}} \cdot \mathbf{F} \right] : [\mathbf{S}_{\mathrm{eq}} + \mathbf{S}_{\mathrm{neq}}] dV. \tag{86}$$

The second phase at the microlevel (index "2") consists of the standard nonlinear elastic material without curing effects. This material is characterized by the same potential as the material at the macrolevel so that the second variation has a form analogous to (82). However, it is here expressed in terms of $\tilde{\mathbf{w}}$ and $\overline{\mathbf{F}}$, and the increment of the variation of the internal energy and the residual are written separately

$$\begin{aligned}
\Delta\delta\Pi_2 = &\int_{V_2} \mathrm{Grad}\delta\tilde{\mathbf{w}} : [\mathrm{Grad}\Delta\tilde{\mathbf{w}} \cdot [\mathbf{S}_{\mathrm{dev}} + \mathbf{S}_{\mathrm{vol}}]] dV \\
&+ \int_{V_2} \left[\mathrm{Grad}^{\mathrm{T}}\delta\tilde{\mathbf{w}} \cdot \mathbf{F} \right] : [\mathbb{E}_{\mathrm{dev}} + \mathbb{E}_{\mathrm{vol}}] : \left[\mathbf{F}^{\mathrm{T}} \cdot \mathrm{Grad}\Delta\tilde{\mathbf{w}} \right] dV \\
&+ \int_{V_2} \left[\left[\mathrm{Grad}^{\mathrm{T}}\delta\tilde{\mathbf{w}} \cdot \mathbf{F} \right] : J\mathbf{C}^{-1} \left[\frac{1}{V_2} \frac{\partial^2 \Psi_{vol}}{\partial\theta^2} \right] \right. \\
&\times \left. \int_V J\mathbf{C}^{-1} : \left[\mathbf{F}^{\mathrm{T}} \cdot \mathrm{Grad}\Delta\tilde{\mathbf{w}} \right] dV \right] dV,
\end{aligned} \tag{87}$$

$$\delta_{\tilde{\mathbf{w}}}\Pi_2^{\mathrm{res}}(\tilde{\mathbf{w}},\overline{\mathbf{F}}) = \int_{V_2} \left[\mathrm{Grad}^{\mathrm{T}}\delta\tilde{\mathbf{w}} \cdot \mathbf{F} \right] : [\mathbf{S}_{\mathrm{dev}} + \mathbf{S}_{\mathrm{dev}}] dV. \tag{88}$$

Finally, taking both phases and the corresponding expressions (85)–(88) into account, the complete microscopic BVP can be expressed in the form

$$\Delta\delta\Pi_1 + \Delta\delta\Pi_2 = -\delta_{\tilde{\mathbf{w}}}\Pi_1^{\mathrm{res}}(\tilde{\mathbf{w}},\overline{\mathbf{F}}) - \delta_{\tilde{\mathbf{w}}}\Pi_2^{\mathrm{res}}(\tilde{\mathbf{w}},\overline{\mathbf{F}}), \tag{89}$$

$$\tilde{\mathbf{w}}^{+} = \tilde{\mathbf{w}}^{-}, \quad \delta\tilde{\mathbf{w}} = \mathbf{0}, \quad \Delta\tilde{\mathbf{w}} = \mathbf{0} \quad \text{on } \partial\mathcal{B}, \tag{90}$$

where Eq. (90) represents the periodic boundary conditions derived from the Hill macrohomogeneity condition (8). A more general formulation convenient for a multiphase material is now straightforward

$$\sum_i^n \Delta\delta\Pi_i = -\sum_i^n \delta_{\tilde{\mathbf{w}}}\Pi_i^{\mathrm{res}}(\tilde{\mathbf{w}},\overline{\mathbf{F}}), \tag{91}$$

$$\tilde{\mathbf{w}}^{+} = \tilde{\mathbf{w}}^{-}, \quad \delta\tilde{\mathbf{w}} = \mathbf{0}, \quad \Delta\tilde{\mathbf{w}} = \mathbf{0} \quad \text{on } \partial\mathcal{B}. \tag{92}$$

Here, symbol n represents the number of different phases and the boundary conditions (90) are unchanged.

For the solution of the BVP (89) and (90), the multiscale program MSFEAP is used (Ilic, 2010). This program is written by using the standard FE code FEAP (Taylor, 2011) as the basis, and it allows the solution of different problems from the macroscopic as well as from the microscopic point of view.

8. Numerical examples

The numerical simulations which will be presented in this section demonstrate the influence of the viscous and shrinkage effects on the behavior of homogeneous and microheterogeneous curing materials. Moreover, they are conducted such that a comparison with the results for elastic curing (Klinge, 2012) is easily possible.

8.1. Time-dependent material properties

The modeling of the viscoelastic curing accompanied by shrinkage requires data on several time-dependent material parameters: the shear modulus μ and Poisson's ratio ν are relevant for describing the elastic part of the curing process, the relaxation time T regulates the evolution of viscous deformations and the degree of cure α influences the intensity of the shrinkage. Since the process is characterized by a smooth change of material properties, the exponential saturation functions are chosen for simulating the evolution of material parameters

$$\mu(t) = \mu_0 + [\mu_\infty - \mu_0][1 - \exp(-\varkappa_\mu t)], \tag{93}$$

$$\nu(t) = \nu_0 + [\nu_\infty - \nu_0][1 - \exp(-\varkappa_\nu t)], \tag{94}$$

$$T(t) = T_0 + [T_\infty - T_0][1 - \exp(-\varkappa_T t)], \tag{95}$$

$$\alpha(t) = \alpha_0 + [\alpha_\infty - \alpha_0][1 - \exp(-\varkappa_\alpha t)]. \tag{96}$$

Here, index "0" denotes the initial value, index "∞" is related to the final value while $\varkappa$ determines the curvature of the corresponding exponential function. More details of the experimental results for the elastic material parameters μ and ν are explained in the work of Kiasat (2000). It should also be pointed out that the free energy density (44) depends on the bulk modulus which is calculated as follows

$$\kappa(t) = \frac{2}{3}\left[\frac{\mu_\infty[1+\nu_\infty]}{1-2\nu_\infty} + \frac{3e^{\frac{t[1-2\nu_\infty]\varkappa_\nu}{-1+2\nu_0}}[\nu_0-\nu_\infty]\left[\mu_\infty[-1+2\nu_0]\varkappa_\mu + \mu_0[1-2\nu_\infty]\varkappa_\nu\right]}{[-1+2\nu_0][-1+2\nu_\infty]\left[[-1+2\nu_0]\varkappa_\mu + [1-2\nu_\infty]\varkappa_\nu\right]} - \frac{e^{-t\varkappa_\mu}[\mu_0-\mu_\infty]\left[[1+\nu_0]\varkappa_\mu - [1+\nu_\infty]\varkappa_\nu\right]}{[-1+2\nu_0]\varkappa_\mu + [1-2\nu_\infty]\varkappa_\nu}\right]. \tag{97}$$

The expression above is obtained by using the correspondence principle and the assumptions (93) and (94), which is briefly explained in B. Alternatively, the bulk modulus can also be calculated according to the following recurrence formula

$$\kappa(t_n) = \frac{1}{3[1-\nu_0-\nu(t_n-t_{n-1})]}\left[\mu(t_n)[2+\nu_0+\nu(t_n-t_{n-1})] + [\mu_0+3\kappa_0][\nu(t_n)-\nu(t_n-t_1)] + \sum_{i=1}^{n-1}[\mu(t_i)+3\kappa(t_i)][\nu(t_n-t_{i-1})-\nu(t_n-t_{i+1})]\right] \tag{98}$$

where the standard relationship valid in the elasticity theory applies for the initial value

$$\kappa_0 = \frac{2\mu_0(1+\nu_0)}{3(1-2\nu_0)}. \tag{99}$$

An important advantage of the numerical solution (98) in the comparison with (97) is that it depends only on the discrete values of μ and ν and thus can be applied for any expression determining these two material parameters. The derivation of (98) is presented in C.

Apart from the time-dependent material parameters, the simulations of curing polymers still depend on the elastic constants μ_e and ν_e regulating the non-equilibrium free energy density, and on the magnitude of shrinkage s. In the examples concerned with microheterogeneous materials, an additional elastic phase is introduced. For its simulation, two elastic time-independent material parameters are needed.

Before discussing of the numerical examples, it should still be mentioned that the academic examples are considered in the following sections. Here, the material parameters are chosen such that the characteristic phenomena are clearly presented and compared. A precise determination of constants typical of some particular kinds of polymers is envisaged as a possible topic of the future work concerned with the inverse analysis.

8.2. Modeling of homogeneous polymers

In this section, the focus is firstly placed on viscous effects and the shrinkage of homogeneous polymers. The former are illustrated on the basis of a tension test applied to a rectangle sample with the dimensions 300 mm × 100 mm (Fig. 2a). During this test, the left boundary is fixed while the horizontal displacements on the right boundary are prescribed. The displacement function U includes two phases with increasing load and two holding phases with constant load (Fig. 2b). The test is applied to the samples consisting of different materials, and the calculated stresses are used to qualify the influence of individual material parameters.

The first group of results obtained here deals with stress distribution over the sample for four time steps in which the individual loading phases start or finish (Fig. 3). The comparison of Fig. 3a and b (or alternatively Fig. 3c and d) indicates that the viscoelastic curing, in contrast to elastic curing (Klinge, 2012), is characterized by

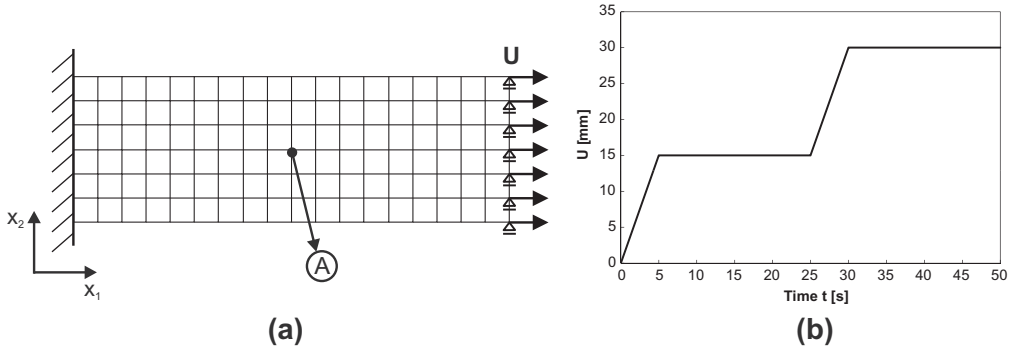

Fig. 2. (a) Tension test for a rectangular plate. (b) Displacement function U.

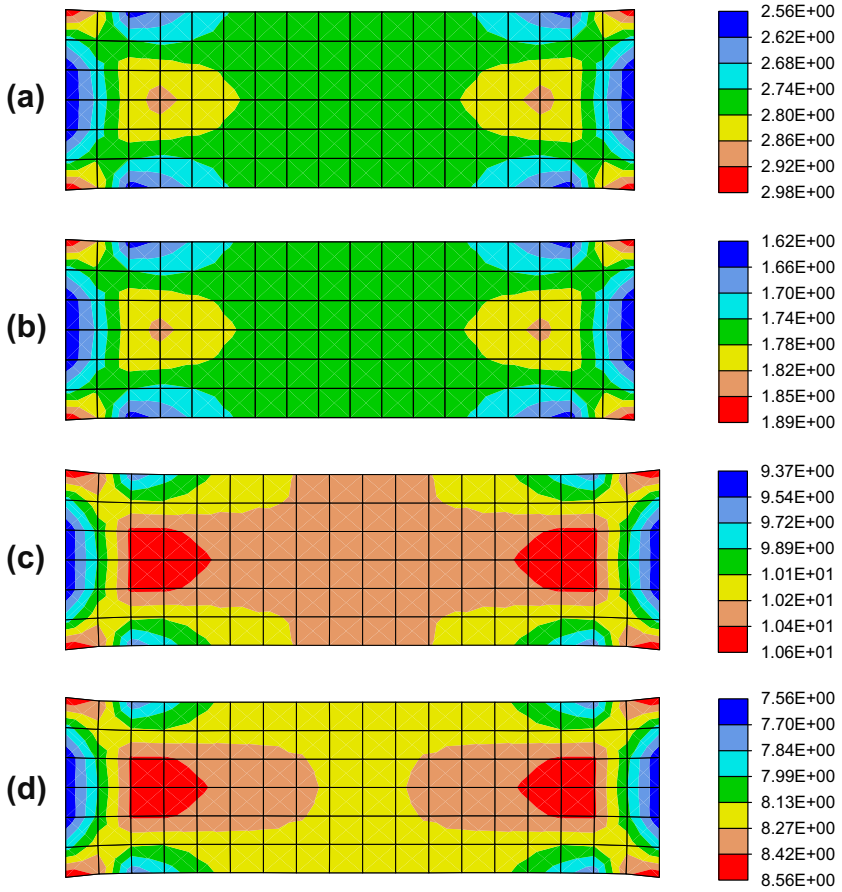

Fig. 3. Stress distribution in X_1-direction after: (a) 5 s; (b) 25 s; (c) 30 s; (d) 50 s. The stresses are expressed in MPa. Applied material parameters: $\mu_0 = 0.01$ MPa, $\mu_\infty = 50$ MPa, $\varkappa_\mu = 0.0925\ s^{-1}$, $\nu = 0.35$, $T_0 = 0.01$ s, $T_\infty = 5$ s, $\varkappa_T = 0.0925\ s^{-1}$, $\mu_e = 25$ MPa, $\nu_e = 0.35$.

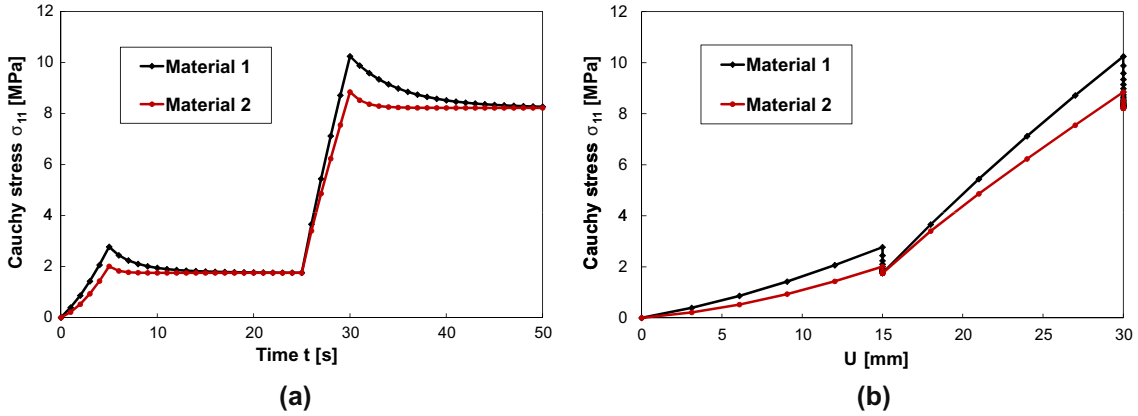

Fig. 4. (a) Cauchy stress σ_{11} vs. time, (b) Cauchy stress σ_{11} vs. displacement function U. Material 1: $T_\infty = 5$ s. Material 2: $T_\infty = 1$ s. Remaining material parameters: $\mu_0 = 0.01$ MPa, $\mu_\infty = 50$ MPa, $\varkappa_\mu = 0.0925\ s^{-1}$, $\nu = 0.35$, $T_0 = 0.01$ s, $\varkappa_T = 0.0925\ s - 1$, $\mu_e = 25$ MPa, $\nu_e = 0.35$.

the stress change during the holding phases. This observation is even more distinct if the stress state at an individual point is studied. For this purpose, point A in the middle of the sample (Fig. 2) is chosen and the stress state with respect to the time and with respect to the applied displacements is monitored (Fig. 4). Two kinds of materials with different relaxation times are simulated and both resulting diagrams show similar properties: Since the first loading phase coincides with the beginning and the second loading phase with the middle of the curing process, the time-dependent material parameters evolve fast and the stress response in both loading phases is nonlinear. The shear modulus in the second loading phase has a higher value so that the stress rate here is noticeably higher. At the end of each loading phase, the stress reaches the local maximum. However, it gradually increases during the holding phase which is known as the relaxation phenomenon. At the end of this phase the stress state tends to the stationary value coinciding with the value typical of the curing process without considering viscous effects. The comparison of diagrams corresponding to different materials indicates that the lower relaxation time is related to less distinct viscous effects.

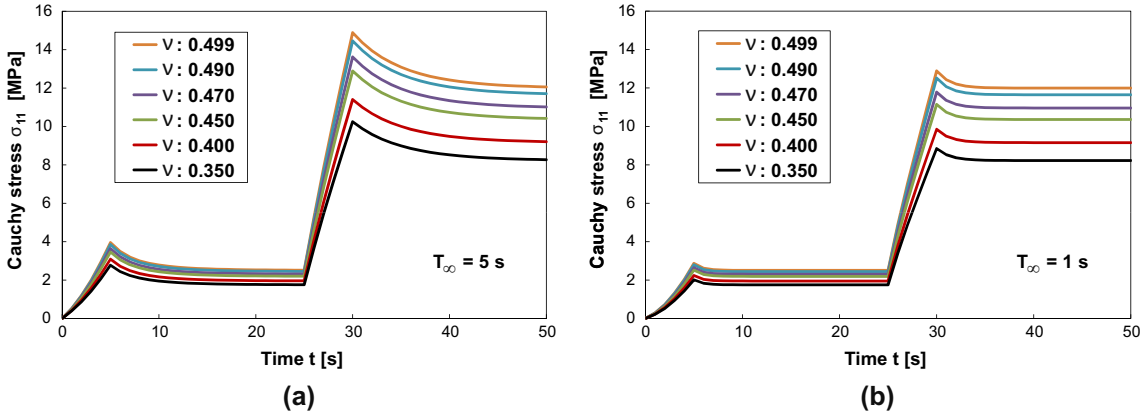

Fig. 5. Cauchy stress at point A for materials with different Poisson's ratio. (a) $T_\infty = 5$ s. (b) $T_\infty = 1$ s. The remaining parameters apply to both materials: $\mu_0 = 0.01$ MPa, $\mu_\infty = 50$ MPa, $\varkappa_\mu = 0.0925\ s^{-1}$, $\nu = 0.35$, $T_0 = 0.01$ s, $\varkappa_T = 0.0925\ s^{-1}$, $\mu_e = 25$ MPa, $\nu_e = 0.35$.

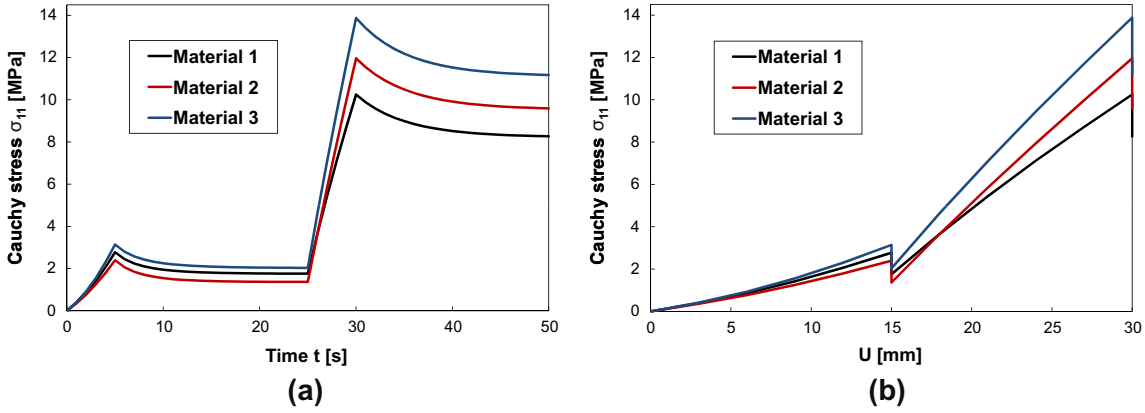

Fig. 6. Comparison of the stress state for one material with constant and two materials with time-dependent Poisson's ratio. Material 1 possesses constant Poisson's ratio: $\nu = 0.35$. Material 2 possesses time-dependent Poisson's ratio: $\nu_0 = 0.01$, $\nu_\infty = 0.499$, $\varkappa_\nu = 0.0925$. Material 3 also possesses time-dependent Poisson's ratio: $\nu_0 = 0.4$, $\nu_\infty = 0.499$, $\varkappa_\nu = 0.0925$. Remaining material parameters: $\mu_0 = 0.01$ MPa, $\mu_\infty = 50$ MPa, $\varkappa_\mu = 0.0925\ s^{-1}$, $T_0 = 0.01$ s, $T_\infty = 5$ s, $\varkappa_T = 0.0925\ s^{-1}$, $\mu_e = 25$ MPa, $\nu_e = 0.35$.

The influence of Poisson's ratio is checked in the analogous way: the test shown in Fig. 2 is repeated for materials with different values of this parameter lying in the range 0.35–0.499. The subsequent comparison of corresponding diagrams leads to the conclusion that higher Poisson's ratio corresponds to higher stresses (Fig. 5a). This conclusion remains valid for materials with different relaxation time (Fig. 5b).

The influence of the Poisson ratio is also investigated on the basis of an example in which the behavior of a material with constant Poisson's ratio (Material 1) is compared to the behavior of two materials with time-dependent Poisson's ratio (Materials 2 and 3) (Fig. 6). Poisson's ratio of Material 2 has an initial value of 0.01 and grows up to the value of 0.499 while Poisson's ratio of Material 3 changes from 0.4 to 0.499. The results for Materials 1 and 2 show that the stresses for the sample consisting of Material 1 are higher at the beginning of the curing, whereas the situation is opposite in the final phase. This endorses the conclusion that a neglecting of the evolution of Poisson's ratio might lead to a significant underestimation of the stress values at the end of the curing process. The same observation has been made when solely the elastic aspects of the curing were studied (Klinge, 2012). Due to the high values of Poisson's ratio in the case of Material 3, the stresses corresponding to this material type are permanently higher than those in the other two cases.

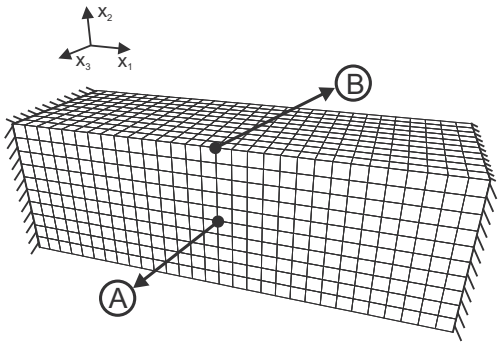

Fig. 7. Geometry of the sample and the boundary conditions applied for the shrinkage test.

The final example studying the behavior of homogeneous polymers deals with the effects of shrinkage. Since this is an autogeneous process, the material behavior without the influence of an external load is observed. The chosen sample is a parallelepiped with dimensions 300 mm × 100 mm × 100 mm both vertical faces of which are fixed (Fig. 7).

The investigation encompasses three different viscoelastic curing polymers with different relaxation times (Fig. 8a). The obtained

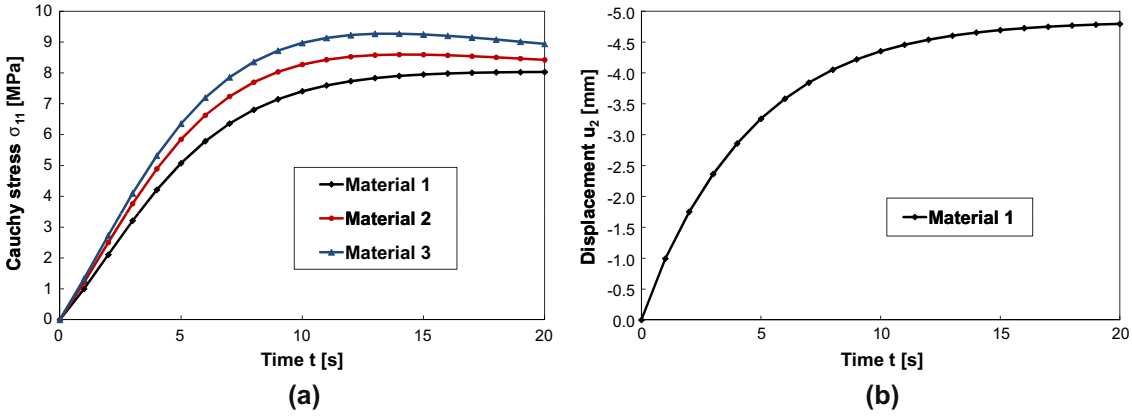

Fig. 8. (a) Stress distribution σ_{11} at point A. (b) Displacements in X_2-direction at point B. Material 1: $T_\infty = 3$ s. Material 2: $T_\infty = 6$ s. Material 3: $T_\infty = 9$ s. Remaining material parameters: $\mu_0 = 0.01$ MPa, $\mu_\infty = 50$ MPa, $\varkappa_\mu = 0.25\ s^{-1}$, $\nu = 0.35$, $T_0 = 0.01$ s, $\varkappa_T = 0.25\ s^{-1}$, $\mu_e = 25$ MPa, $\nu_e = 0.35$, $\alpha_0 = 0.01$, $\alpha_\infty = 1$, $\varkappa_\alpha = 0.25\ s^{-1}$, $s = -0.2$.

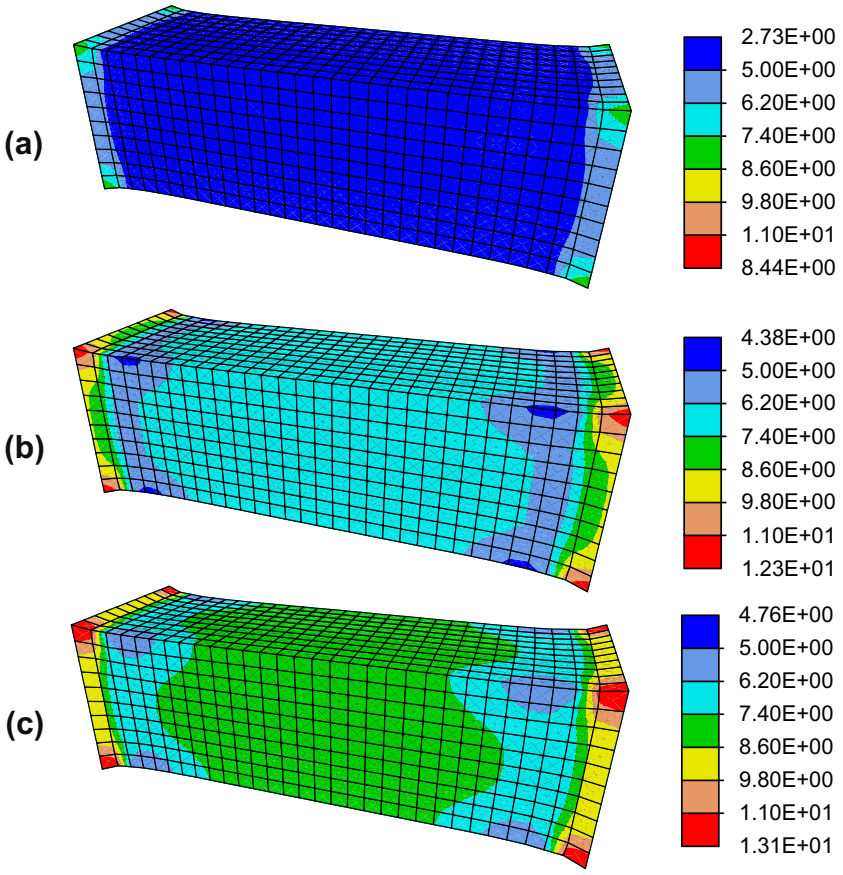

Fig. 9. Distribution of σ_{11}-stress for time steps: (a) 5 s; (b) 10 s; (c) 20 s. Stresses are expressed in MPa. Applied material parameters: $\mu_0 = 0.01$ MPa, $\mu_\infty = 50$ MPa, $\varkappa_\mu = 0.25\ s^{-1}$, $\nu = 0.35$, $T_0 = 0.01$ s, $T_\infty = 3$ s, $\varkappa_T = 0.25\ s^{-1}$, $\mu_e = 25$ MPa, $\nu_e = 0.35$, $\alpha_0 = 0.01$, $\alpha_\infty = 1$, $\varkappa_\alpha = 0.25\ s^{-1}$, $s = -0.2$.

values show that the stress rate (at point A) in the first phase (1–10 s) of curing is high. Different from this, the later stage of curing is characterized by a slow increase of stress which now tends to a stationary value. Higher values of the relaxation time manifest through higher values of stresses. The deformations at point B are graphically represented in Fig. 8b. They show a behavior similar to the stresses: fast growth at the beginning and a gradual decrease of the rate in the second phase. The values corresponding to different materials are close so that only one material type is chosen for the illustration. The stress values corresponding to the complete sample are presented in Fig. 9. Here, the highest values occur on the fixed boundaries while a rather homogeneous stress state is characteristic of the middle part of the sample.

8.3. Modeling of microheterogeneous materials

The modeling of microheterogeneous polymers is illustrated on the basis of examples used to investigate the combination of a curing material with a nonlinear elastic material. In most simulations, it is assumed that the additional phase has a high stiffness which

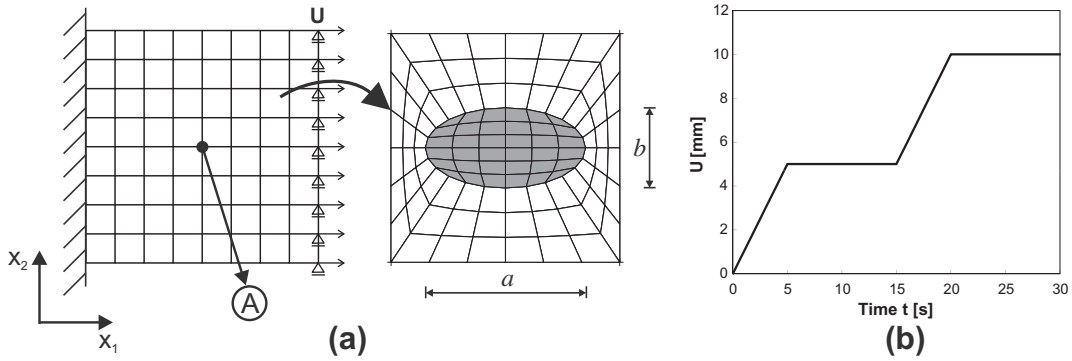

Fig. 10. (a) The macroscopic tension test and the RVE associated to each Gauss point. (b) Time history of prescribed macrodisplacements.

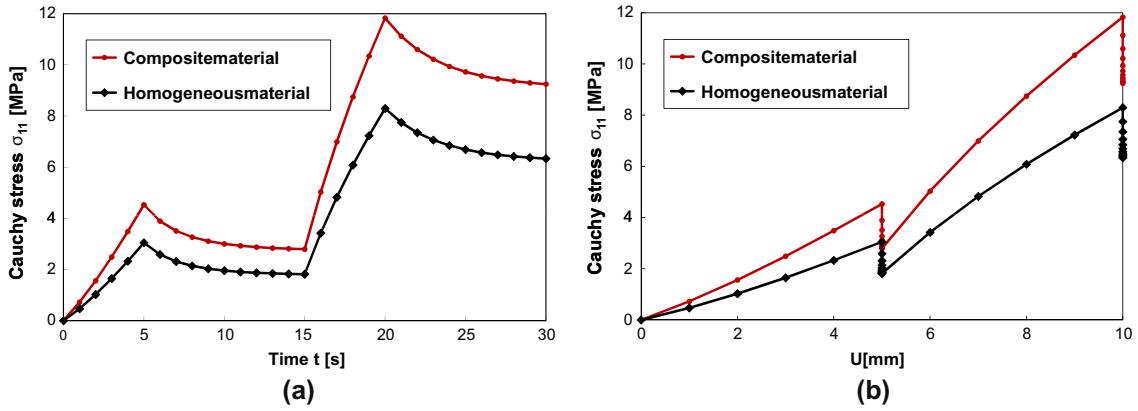

Fig. 11. Comparison of the stress state for a microheterogeneous and a homogeneous material at point A. The RVE of the microheterogenous material consists of matrix material with embedded inclusions. The homogeneous material consists only of the matrix material. Matrix material: $\mu_0 = 0.01$ MPa, $\mu_\infty = 50$ MPa, $\varkappa_\mu = 0.15\ s^{-1}$, $\nu = 0.35$, $T_0 = 0.01$ s, $T_\infty = 3$ s, $\varkappa_T = 0.15\ s^{-1}$, $\mu_e = 30$ MPa, $\nu_e = 0.35$. Inclusion $\mu = 500$ MPa, $\nu = 0.35$.

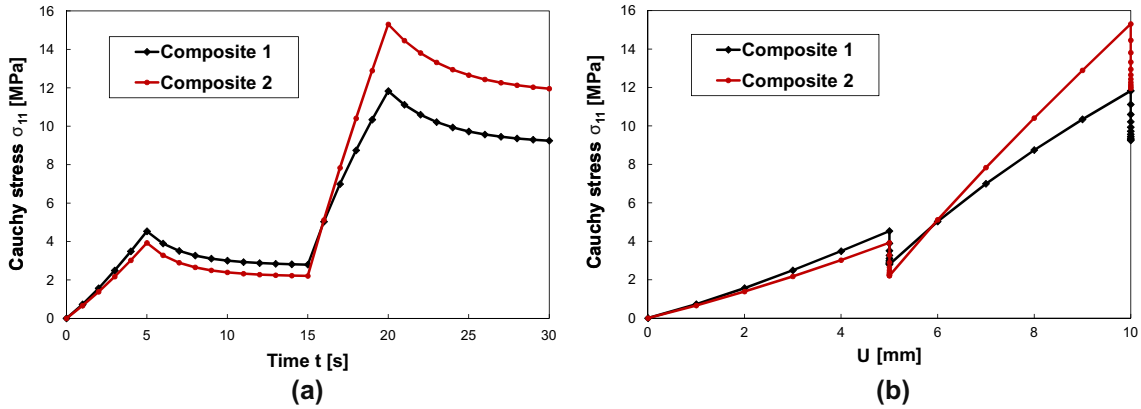

Fig. 12. Influence of time-dependent Poisson's ratio to the stress state at point A. Composite 1 contains matrix material with constant Poisson's ratio $\nu = 0.35$. Composite 2 contains matrix material with time-dependent Poisson's ratio: $\nu = 0.01$, $\nu_\infty = 0.499$, $\varkappa_\nu = 0.15\ s^{-1}$. Remaining parameters of both matrix materials: $\mu_0 = 0.01$ MPa, $\mu_\infty = 30$ MPa, $\varkappa_\mu = 0.15\ s^{-1}$, $T_0 = 0.01$ s, $T_\infty = 3$ s, $\varkappa_T = 0.15\ s^{-1}$, $\mu_e = 30$ MPa, $\nu_e = 0.35$. Both materials have the same type of inclusions with the parameters $\mu = 500$ MPa, $\nu = 0.35$.

corresponds to the case of reinforced materials, a group of nowadays widely applied materials. However, the model is general and can also be applied for alternative combinations.

The initial examples in this section deal with viscoelastic curing without considering shrinkage. Here, the macroscopic test is concerned with a square plate of dimensions 100 mm × 100 mm (Fig. 10a). Similarly to the situation presented in Fig. 2, the displacements on the left boundary as well as the vertical displacements on the right boundary of this plate are constrained while the horizontal displacements on the right boundary are prescribed (Fig. 10b). The macroscopic plate is discretized by four-node elements with four Gauss points to which the RVEs determining the material microstructure are associated. A single RVE has the form of a square with a side length of 1 mm and contains an elliptic

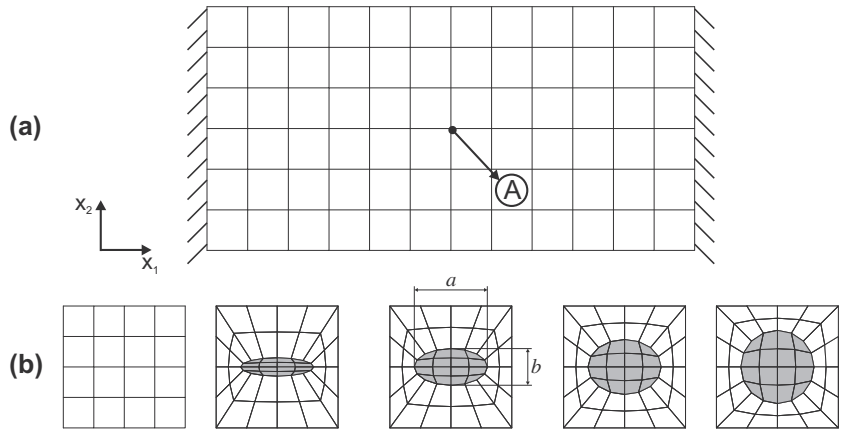

Fig. 13. Macroscopic specimen and the RVEs with different volume fractions of the non-shrinking material.

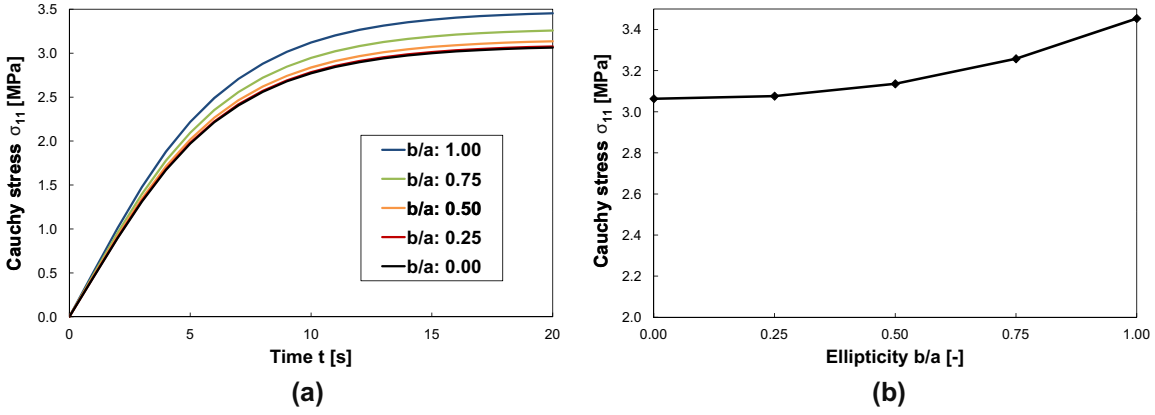

Fig. 14. (a) Cauchy stress σ_{11} vs. time, (b) Cauchy stress σ_{11} for the time step $t = 1$ s vs. ellipticity of the inclusion. Inclusion with high stiffness: $\mu = 500$ MPa, $\nu = 0.35$. Matrix material: $\mu_0 = 0.01$ MPa, $\mu_\infty = 30$ MPa, $\varkappa_\mu = 0.25\ \mathrm{s}^{-1}$, $\nu = 0.35$, $T_0 = 0.01$ s, $T_\infty = 1$ s, $\kappa_T = 0.25\ \mathrm{s}^{-1}$, $\mu_e = 30$ MPa, $\nu_e = 0.35$, $\alpha_0 = 0.01$; $\alpha_\infty = 1$, $\varkappa_\alpha = 0.25\ \mathrm{s}^{-1}$, $s = -0.1$.

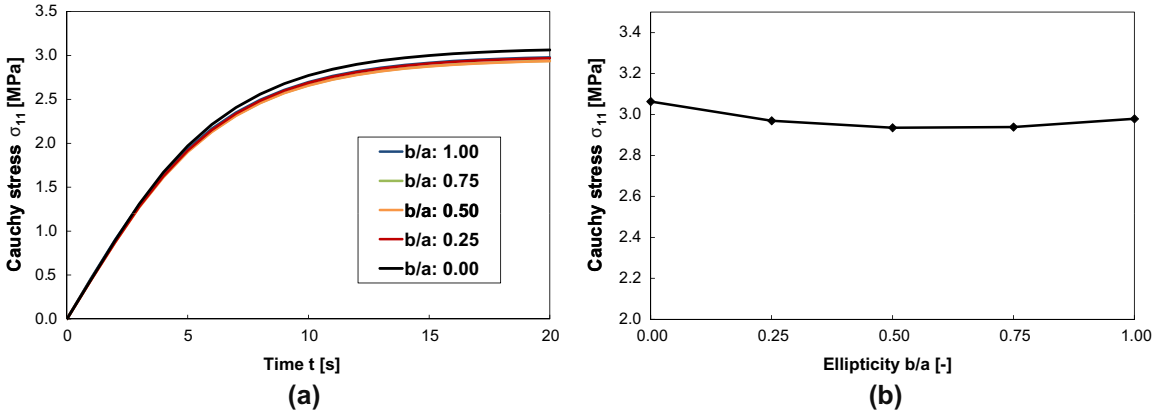

Fig. 15. (a) Cauchy stress σ_{11} vs. time, (b) Cauchy stress σ_{11} for the time step $t = 1$ s vs. ellipticity of the inclusion. Inclusion with moderate stiffness: $\mu = 90$ MPa, $\nu = 0.35$. The properties of the matrix material are the same as those cited in the caption of Fig. 14.

inclusion whose major and minor axis amount to $a = 0.7$ mm and $b = 0.35$ mm, respectively. While the matrix material consists of viscous curing material, the inclusion consists of purely nonlinear elastic material.

The numerical values presented in Fig. 11 endorse the expectations. Because of the high stiffness of the inclusion, the prescribed deformations cause higher stresses in the heterogeneous material than in the homogeneous material. The remaining properties of the viscoelastic response remain unchanged in comparison with the results that were explained in the section devoted to the singlescale simulations (Fig. 4). The loading phases are characterized by a nonlinear increase and the holding phases by the stress relaxation. The influence of time-dependent Poisson's ratio on the effective behavior of a microheterogeneous polymer is presented in

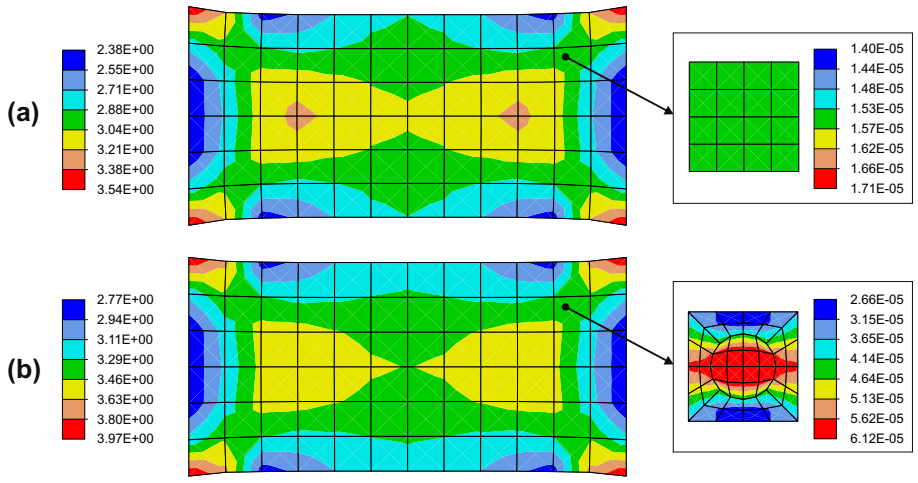

Fig. 16. State of stresses σ_{11} in [MPa] for a homogeneous material and a material with circular inclusion. Inclusion: $\mu = 500$ MPa, $\nu = 0.35$. Matrix material: $\mu_0 = 0.01$ MPa, $\mu_\infty = 30$ MPa, $\varkappa_\mu = 0.25\ s^{-1}$, $\nu = 0.35$, $T_0 = 0.01$ s, $T_\infty = 1$ s, $\varkappa_T = 0.25\ s^{-1}$, $\mu_e = 30$ MPa, $\nu_e = 0.35$, $\alpha_0 = 0.01$, $\alpha_\infty = 1$, $\varkappa_\alpha = 0.25\ s^{-1}$, $s = -0.1$. The time step $t = 1$ s.

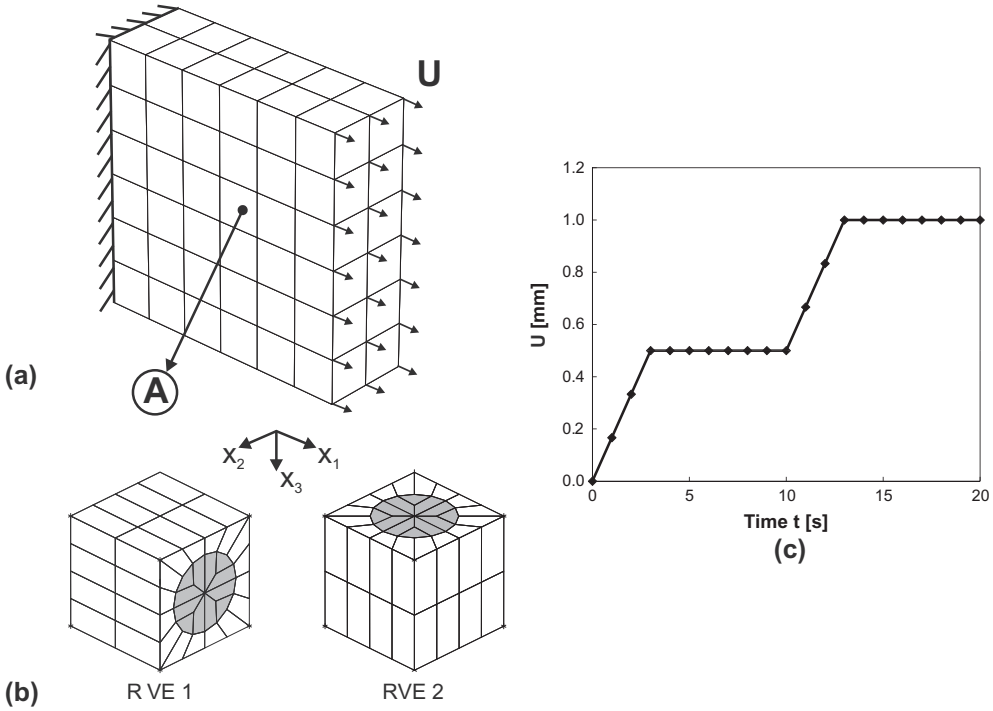

Fig. 17. (a) Macroscopic tension test. (b) Different orientations of the RVE. (c) Displacement function U.

Fig. 12. The results indicate that this parameter causes the strong increase of stresses in the last phase of the curing process.

The example chosen for studying the shrinkage of microheterogeneous polymers is presented in Fig. 13a. The assumed macroscopic sample has dimensions 100 mm × 50 mm and is discretized by a mesh with 12 × 6 elements. Its vertical faces are fixed but no external load is applied. The focus of studies is placed on the influence of the volume fraction of an additional non-shrinking material on the intensity of shrinkage and stresses. For this purpose, five sorts of materials with different ellipticities of the inclusion are tested (Fig. 13b). Two groups of simulations with a duration of 20 s are conducted. In the first case the inclusion consists of a material with very high stiffness (μ = 500 MPa). In the second case the inclusion with moderate stiffness (μ = 90 MPa) is chosen. In both cases the matrix material has the same properties.

The results of simulations performed are presented in Figs. 14 and 15. A comparison of the stress states at a single point A for both sets of material parameters yields the following conclusion: In case of the very high stiffness, the increasing volume fraction of the inclusion is related to the increase of the stress values (Fig. 14). The situation is opposite if the stiffness of the inclusion is moderate. In this case, the increase of the volume fraction of the inclusion causes the decrease of the volume fraction of the shrinking matrix material. As a consequence, the total deformations and stresses decrease as well (Fig. 15).

In addition to the stress state for a single point which is shown in Figs. 14 and 15, the stress distribution over the complete sample is presented in Fig. 16. The chosen examples are concerned with the stress state for a homogeneous material and for the material with a circular inclusion after the first second of the curing $t = 1$ s.

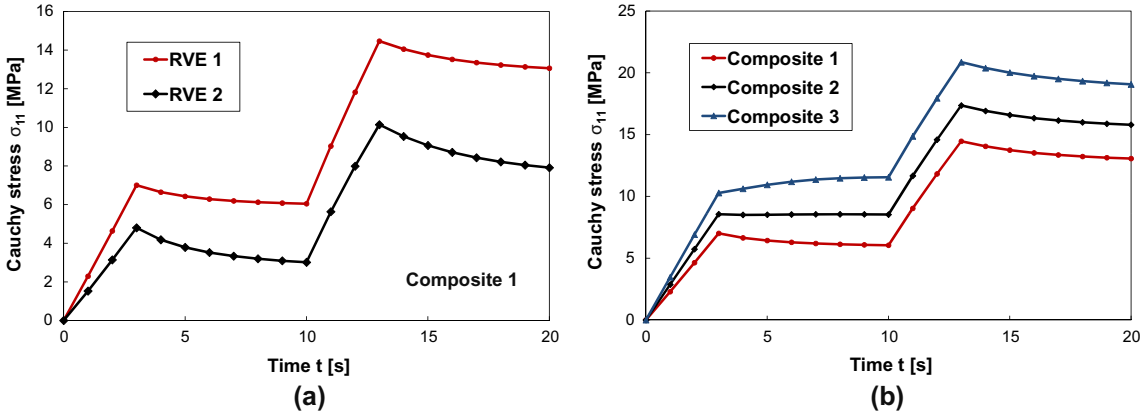

Fig. 18. (a) Comparison of the stress state for the orientations of the RVE shown in Fig. 17. (b) Influence of shrinkage on total stresses. Composite 1 has the matrix material with $s = 0$ (non-shrinking mat.). Composite 2 has the matrix material with $s = -0.1$ (shrinking mat.). Composite 3 has the matrix material with $s = -0.2$ (shrinking mat.). Remaining parameters of all three matrix materials: $\mu_0 = 0.01$ MPa, $\mu_\infty = 30$ MPa, $\varkappa_\mu = 0.25\ s^{-1}$, $\nu = 0.35$, $T_0 = 0.01$ s, $T_\infty = 3$ s, $\varkappa_T = 0.25\ s^{-1}$, $\mu_e = 45$ MPa, $\nu_e = 0.35$, $\alpha_0 = 0.01$, $\alpha_\infty = 1$, $\varkappa_\alpha = 0.25\ s^{-1}$. Fibers have the same properties in all cases: $\mu = 150$ MPa, $\nu = 0.35$.

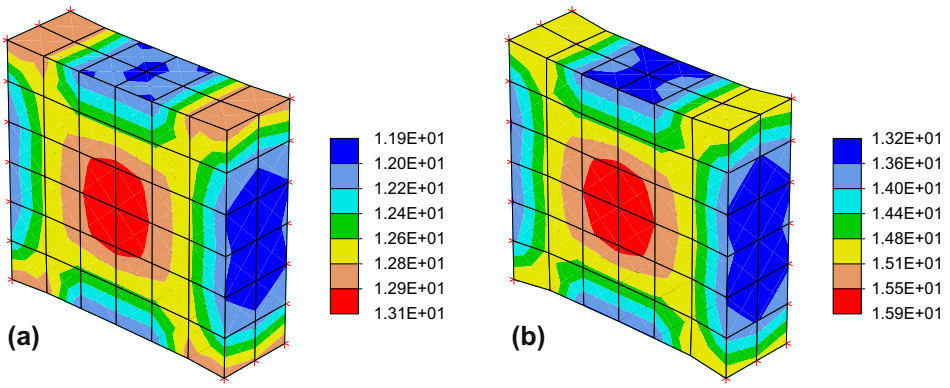

Fig. 19. Stress component σ_{11} at the end of the curing process. (a) Composite 1. (b) Composite 2. Material properties are the same as cited in the caption of Fig. 18.

The final example in this work is used to demonstrate the material anisotropy of microheterogeneous polymers as well as to give an insight into the contribution of shrinkage to the total stresses. The mentioned effects are studied on the basis of a test, considering a material with long fiber reinforcement (Fig. 17a and b). The chosen 3D sample has the dimensions 300 mm × 10 mm × 30 mm and is discretized by a mesh with 72 elements. One vertical face of the sample is fixed and the horizontal displacements on the second vertical face are prescribed. The loading function has four phases: two pull- and two holding phases. The curing time amounts to 20 s (Fig. 17c).

Two tests are conducted in order to study the material anisotropy. In the first case, the orientation of the fiber is assumed to be parallel to the applied load and in the second case perpendicular to this direction (Fig. 17b). At this stage, a viscoelastic curing material without shrinkage is assumed as the matrix material while the inclusion consists of a nonlinear elastic material. The RVE has the form of a cube with the side length of 1 mm and the radius of the fiber amounts to 0.35 mm. The macroscopic stress state at point A for both orientations of the RVE is presented in Fig. 18a. Obviously, the stress state for the horizontal direction of fibers is higher than in the case where the vertical fibers are used. It can also be noted that, due to the high stiffness of the fiber, the nonlinearity of the loading phases of the diagram are less distinct than in the case of homogeneous materials (Fig. 4).

The study of the influence of shrinkage on the total stresses is performed on the basis of an example in which the behavior of three composite materials is compared (Fig. 18b). The matrix material of Composite 1 is viscoelastic material while the matrix materials of the remaining two composites (Composite 1 and Composite 2) are viscoelastic shrinking materials with different magnitudes of shrinkage s. The horizontal fiber orientation is assumed in all cases. The results show that a higher magnitude of shrinkage s is accompanied by the higher stresses. In the case of Composite 2, the shrinkage at the beginning of the curing process reduces the influence of the relaxation so that an almost constant plateau is obtained for the first holding phase. For Composite 3, the initial shrinkage has such a strong influence that the stresses are increasing during the first holding phase. During the second holding phase, the curing is almost finished and the shrinkage effects are negligible. The relaxation here is easily noticeable. The last figure (Fig. 19) compares the stress distribution at the end of the curing process for two macroscopic plates consisting of two different materials.

9. Conclusions

The aim of this work was to present a multiscale model for the curing of polymers in which the focus is placed on the simulation

of viscous and shrinkage effects. The implementation of viscous effects is based on the decomposition of the free energy density into an equilibrium and a non-equilibrium part. The former depends on the total deformation and on time-dependent material parameters. It consists of two convolution integrals corresponding to the deviatoric and the volumetric deformations. The non-equilibrium part is formulated in terms of elastic deformations and constant material parameters. The extension related to the shrinkage effects uses the decomposition of the deformation gradient into a mechanical and shrinkage part and does not require any reformulation of the energy expression. The developed model together with the multiscale FEM program MSFEAP is applied for modeling the microheterogeneous materials. The mentioned program code uses the concept according to which the modeling of a macroscopic body is split into the solution of two BVPs: One related to the simulation of the macroscopic body and another one related to the analysis of the RVE. The boundary conditions for the RVE are derived from the Hill macrohomogeneity condition.

The application of the model is illustrated on the basis of several numerical examples. The viscous effects of homogeneous polymers are investigated by using the tension test in which two loading phases are combined with two holding phases. The stresses corresponding to loading phases show the same feature as in the case of elastic curing, namely the nonlinear growth due to the time evolving material parameters. The new effect observed here is the stress decrease during the holding phase, which is known as the relaxation. The shrinkage effects are studied on the basis of a test in which the stresses in a parallelepiped with two fixed faces are monitored. The obtained numerical results show an increase of stress without the application of any external load. Furthermore, the simulation of the shrinkage together with the mechanical influences indicates that this phenomenon can eliminate the relaxation effects and cause a slight increase of stresses during the holding phase. The multiscale examples deal with macroscopic tests analogous to those conducted in the singlescale simulations. However, here, an RVE is applied in order to depict the material microstructure. In most cases, the combination of a curing material with an elastic material of constant properties is considered, but the concept is a general one and can be applied for other combinations as well. The results endorse the expectation that the higher stresses will correspond to the higher stiffness of the additional phase if the same deformations are prescribed. As opposed to this, the additional phase can strengthen or alleviate the shrinkage effects and the corresponding stresses, depending on the volume fraction and the type.

The achieved results certainly indicate that the model can be applied successively for single- and multiscale simulations. However, a determination of material parameters on the basis of experimental investigation might be an important task for the future since the results are strongly dependent on the assumed evolution laws. An optimization of the homogenization procedure in regard of computational time and required computer capacity is an open issue as well.

Appendix A. Derivation of the evolution equation

Within the numerical examples which are presented in Section 8, it is supposed that the evolution of inelastic deformations is controlled by the linearized solution (33). However, the calculation of the derivative (56) in this case is followed by difficulties, which motivates the derivation of an alternative evolution law. For this purpose, firstly the residual inequality (32)

$$-\frac{\partial \Psi_{\mathrm{neq,dev}}}{\partial \mathbf{C}_{\mathrm{e}}} : \frac{\partial \mathbf{C}_{\mathrm{e}}}{\partial \mathbf{F}_{\mathrm{i}}} \dot{\mathbf{F}}_{\mathrm{i}} \geqslant 0 \tag{A.1}$$

is transformed into the expression

$$\boldsymbol{\tau}_{\mathrm{neq}} : \left[\mathbf{F}_{\mathrm{e}} \cdot \mathrm{sym}(\mathbf{l}_{\mathrm{i}}) \cdot \mathbf{F}_{\mathrm{e}}^{\mathrm{T}}\right] \cdot \mathbf{b}_{\mathrm{e}}^{-1} \geqslant 0, \tag{A.2}$$

where $\mathbf{b}_{\mathrm{e}} = \mathbf{F}_{\mathrm{e}} \cdot \mathbf{F}_{\mathrm{e}}^{\mathrm{T}}$ represents the elastic left Cauchy deformation tensor, $\mathbf{l}_{\mathrm{i}} = \dot{\mathbf{F}}_{\mathrm{i}} \cdot \mathbf{F}_{\mathrm{i}}^{-1}$ is the inelastic velocity gradient and the internal non-equilibrium forces are defined by the relationship

$$\boldsymbol{\tau}_{\mathrm{neq}} = 2\mathbf{F}_{\mathrm{e}} \cdot \frac{\partial \Psi_{\mathrm{neq,dev}}}{\partial \mathbf{C}_{\mathrm{e}}} \cdot \mathbf{F}_{\mathrm{e}}^{\mathrm{T}}. \tag{A.3}$$

One possible solution for the problem (A.2) is proposed by Reese and Govindjee (1998) as follows

$$\left[\mathbf{F}_{\mathrm{e}} \cdot \mathrm{sym}(\mathbf{l}_{\mathrm{i}}) \cdot \mathbf{F}_{\mathrm{e}}^{\mathrm{T}}\right] \cdot \mathbf{b}_{\mathrm{e}}^{-1} = \mathbf{V}^{-1} : \boldsymbol{\tau}_{\mathrm{neq}}. \tag{A.4}$$

Here, $\mathbf{V}^{-1}$ is a rank four positive definite tensor

$$\mathbf{V}^{-1} = \frac{1}{2\eta_D}\left[\mathbf{I}^4 - \frac{1}{3}\mathbf{I} \otimes \mathbf{I}\right] + \frac{1}{9\eta_V}\mathbf{I} \otimes \mathbf{I} \tag{A.5}$$

depending on the deviatoric (η_D) and the volumetric viscosity (η_V) which are possibly deformation-dependent. The first term in (A.5) is the deviatoric projector and the second term is the volumetric projector. Accordingly, the expression on the right-hand side of (A.4) turns into

$$\mathbf{V}^{-1} : \boldsymbol{\tau}_{\mathrm{neq}} = \frac{1}{2\eta_D}\boldsymbol{\tau}_{\mathrm{neq,dev}} + \frac{1}{3\eta_V}\boldsymbol{\tau}_{\mathrm{neq,vol}}. \tag{A.6}$$

Obviously, this is a general solution which also applies to the neo-Hooke material with the deviatoric part of the strain energy density defined by Eq. (45)

$$\Psi_{\mathrm{neq,dev}} = \frac{\mu_{\mathrm{e}}}{2}[\mathbf{C}_{\mathrm{e,iso}} : \mathbf{I} - 3]. \tag{A.7}$$

In this assumption, the standard relationship for the isotropic part of the Cauchy deformation tensor is used $\mathbf{C}_{\mathrm{e,iso}} = J_{\mathrm{e}}^{-\frac{2}{3}}\mathbf{C}_{\mathrm{e}}$, such that the necessary derivative of the strain energy part and subsequently the non-equilibrium forces turn into

$$\frac{\partial \Psi_{\mathrm{neq,dev}}}{\partial \mathbf{C}_{\mathrm{e}}} = -\frac{\mu_{\mathrm{e}}}{6}J_{\mathrm{e}}^{-\frac{2}{3}}\mathrm{tr}\mathbf{C}_{\mathrm{e}}\mathbf{C}_{\mathrm{e}}^{-1} + \frac{\mu_{\mathrm{e}}}{2}J_{\mathrm{e}}^{-\frac{2}{3}}\mathbf{I}, \tag{A.8}$$

$$\boldsymbol{\tau}_{\mathrm{neq}} = -\frac{\mu_{\mathrm{e}}}{3}J_{\mathrm{e}}^{-\frac{2}{3}}\mathrm{tr}\mathbf{C}_{\mathrm{e}}\mathbf{I} + \mu_{\mathrm{e}}J_{\mathrm{e}}^{-\frac{2}{3}}\mathbf{b}_{\mathrm{e}}. \tag{A.9}$$

The last expression can additively be split into a volumetric and a deviatoric part

$$\boldsymbol{\tau}_{\mathrm{neq,vol}} = -\frac{\mu_{\mathrm{e}}}{3}J_{\mathrm{e}}^{-\frac{2}{3}}\mathrm{tr}\mathbf{C}_{\mathrm{e}}\mathbf{I} + \frac{\mu_{\mathrm{e}}}{3}J_{\mathrm{e}}^{-\frac{2}{3}}\mathrm{tr}\mathbf{b}_{\mathrm{e}}\mathbf{I} = \frac{\mu_{\mathrm{e}}}{3}J_{\mathrm{e}}^{-\frac{2}{3}}[\mathrm{tr}\mathbf{b}_{\mathrm{e}} - \mathrm{tr}\mathbf{C}_{\mathrm{e}}]\mathbf{I} = 0, \tag{A.10}$$

$$\boldsymbol{\tau}_{\mathrm{neq,dev}} = \mu_{\mathrm{e}}J_{\mathrm{e}}^{-\frac{2}{3}}\mathbf{b}_{\mathrm{e}} - \frac{\mu_{\mathrm{e}}}{3}J_{\mathrm{e}}^{-\frac{2}{3}}\mathrm{tr}\mathbf{b}_{\mathrm{e}}\mathbf{I}, \tag{A.11}$$

where the volumetric part is equal to zero since it holds that $\mathrm{tr}\mathbf{b}_{\mathrm{e}} = \mathrm{tr}\mathbf{C}_{\mathrm{e}}$. Now, on the basis of relationships (A.10) and (A.11), Eq. (A.6) is adapted for the simulation of materials with the energy density (A.7)

$$\mathbf{V}^{-1} : \boldsymbol{\tau}_{\mathrm{neq}} = \frac{\mu_{\mathrm{e}}}{2\eta_D}J_{\mathrm{e}}^{-\frac{2}{3}}\mathbf{b}_{\mathrm{e}} - \frac{\mu_{\mathrm{e}}}{6\eta_D}J_{\mathrm{e}}^{-\frac{2}{3}}\mathrm{tr}\mathbf{b}_{\mathrm{e}}\mathbf{I} \tag{A.12}$$

and Eq. (A.4) is written in the following form

$$\left[\mathbf{F}_{\mathrm{e}} \cdot \mathrm{sym}(\mathbf{l}_{\mathrm{i}}) \cdot \mathbf{F}_{\mathrm{e}}^{T}\right] \cdot \mathbf{b}_{\mathrm{e}}^{-1} = \frac{\mu_{\mathrm{e}}}{2\eta_D}J_{\mathrm{e}}^{-\frac{2}{3}}\mathbf{b}_{\mathrm{e}} - \frac{\mu_{\mathrm{e}}}{6\eta_D}J_{\mathrm{e}}^{-\frac{2}{3}}\mathrm{tr}\mathbf{b}_{\mathrm{e}}\mathbf{I}. \tag{A.13}$$

The last relation is further transformed by using the fact that the symmetric part of the velocity gradient can be expressed in terms of the rate of the right Cauchy deformation tensor

$$\mathrm{sym}(\mathbf{l}_{\mathrm{i}}) = \frac{1}{2}[\mathbf{l}_{\mathrm{i}} + \mathbf{l}_{\mathrm{i}}] = \frac{1}{2}\mathbf{F}_{\mathrm{i}}^{-\mathrm{T}} \cdot \dot{\mathbf{C}}_{\mathrm{i}} \cdot \mathbf{F}_{\mathrm{i}}^{-1}. \tag{A.14}$$

More precisely, the implementation of (A.14) into (A.13) results in the expression

$$\left[\frac{1}{2}\mathbf{F}_e\cdot\mathbf{F}_i^{-T}\cdot\dot{\mathbf{C}}i\cdot\mathbf{F}_i^{-1}\cdot\mathbf{F}_e^{T}\right]\cdot\mathbf{b}_e^{-1}=\frac{\mu_e}{2\eta_D}J_e^{-\frac{2}{3}}\mathbf{b}_e-\frac{\mu_e}{6\eta_D}J_e^{-\frac{2}{3}}\mathrm{tr}\mathbf{b}_e\mathbf{I} \tag{A.15}$$

whose reformulation yields the final nonlinear evolution equation

$$\dot{\mathbf{C}}_i=\frac{\mu_e}{\eta_D}J_e^{-\frac{2}{3}}\mathbf{C}-\frac{\mu_e}{3\eta_D}J_e^{-\frac{2}{3}}\mathrm{tr}\mathbf{b}_e\mathbf{C}_i. \tag{A.16}$$

Appendix B. Analytical calculation of the bulk modulus

The correspondence or equivalence principle is applied for the evaluation of time-dependent material parameters within the viscoelastic theory. According to this principle, the analogous expressions can be used for an elastic and an viscoelastic problem with the difference that a suitably chosen transform is inserted in the latter case. The final, time-dependent solution is then obtained by inverting the solution calculated in the transform plane. Two types of transform are most commonly applied: the Laplace transform in the case of an impulse load and the Laplace–Carson transform for a step response. These two transforms are related to each other according to the relationship

$$\mathcal{C}(f(t))=u\mathcal{L}(f(t))=u\bar{f}(u)$$

where $\mathcal{C}(\cdot)$ denotes the Carson–Laplace transform and $\mathcal{L}(\cdot)$ and the overbar symbol denote the Laplace transform.

Within the examples presented in Section 8, the time-dependent shear modulus and Poisson's ratio are defined by Eqs. (93) and (94) and the correspondence principle is applied for the evaluation of the bulk modulus. The procedure starts by the implementation of the Laplace–Carson transform into the expression for the bulk modulus typical of the elasticity theory

$$\kappa=\frac{2\mu[1+\nu]}{3[1-2\nu]}\quad\Rightarrow\quad u\bar{\kappa}=\frac{2u\bar{\mu}[1+u\bar{\nu}]}{3[1-2u\bar{\nu}]}\quad\Rightarrow\quad\bar{\kappa}=\frac{2\bar{\mu}[1+u\bar{\nu}]}{3[1-2u\bar{\nu}]}. \tag{A.17}$$

Subsequently, the Laplace transform of the bulk modulus is calculated by using the transforms of functions (93) and (94)

$$\bar{\kappa}(u)=\frac{2\left(\frac{\mu_\infty}{u}-\frac{-\mu_0+\mu_\infty}{u+\varkappa_\mu}\right)\left[1+u\left(\frac{\nu_\infty}{u}-\frac{-\nu_0+\nu_\infty}{u+\varkappa_\nu}\right)\right]}{3\left[1-2u\left(\frac{\nu_\infty}{u}-\frac{-\nu_0+\nu_\infty}{u+\varkappa_\nu}\right)\right]} \tag{A.18}$$

and the final time-dependent solution is obtained by using the inverse transform

$$\begin{aligned}\kappa(t)&=\mathcal{L}^{-1}(\bar{\kappa}(u))\\&=\frac{2}{3}\left[\frac{\mu_\infty[1+\nu_\infty]}{1-2\nu_\infty}+\frac{3e^{\frac{t[1-2\nu_\infty]\varkappa_\nu}{-1+2\nu_0}}[\nu_0-\nu_\infty][\mu_\infty[-1+2\nu_0]\varkappa_\mu+\mu_0[1-2\nu_\infty]\varkappa_\nu]}{[-1+2\nu_0][-1+2\nu_\infty][[-1+2\nu_0]\varkappa_\mu+[1-2\nu_\infty]\varkappa_\nu]}\right.\\&\quad\left.-\frac{e^{-t\varkappa_\mu}[\mu_0-\mu_\infty][[1+\nu_0]\varkappa_\mu-[1+\nu_\infty]\varkappa_\nu]}{[-1+2\nu_0]\varkappa_\mu+[1-2\nu_\infty]\varkappa_\nu}\right].\end{aligned} \tag{A.19}$$

Please note that in general, an inversion process does not yield a solution in a closed form so that a numerical interconversion is necessary (C).

Appendix C. Numerical evaluation of the bulk modulus

The numerical interconversion starts with the expression (A.17) as well as the corresponding analytical procedure. This expression is here rewritten in the form

$$2[1+u\bar{\nu}]\bar{\mu}=3[1-2u\bar{\nu}]\bar{\kappa}, \tag{A.20}$$

such that the individual expressions on both sides of the equality sign can be reformulated by using the transformation rule

$$u\bar{f}_1(u)\bar{f}_2(u)=\mathcal{L}\left[f_1(t)f_2(0)+\int_0^t f_1(v)\frac{df_2(t-v)}{d(t-v)}dv\right]. \tag{A.21}$$

The attention is first paid on the evaluation of the left-hand side expression

$$\mathcal{L}(\alpha(t))=2[1+u\bar{\nu}]\bar{\mu}, \tag{A.22}$$

which after the application of (A.21) yields the relationship

$$\alpha(t)=2(1+\nu_0)\mu(t)-2\int_0^t\mu(v)\frac{d\nu(t-v)}{dv}dv. \tag{A.23}$$

Here, the integral on the right-hand side can be split in n subintegrals

$$\alpha(t_n)=2[1+\nu_0]\mu(t_n)-2\sum_{i=1}^{n}\int_{t_{i-1}}^{t_i}\mu(v)\frac{d\nu(t_n-v)}{dv}dv. \tag{A.24}$$

Furthermore, each of the subintegrals is evaluated under the assumption that the intervals $[t_{i-1},t_i]$ are small and that the function $\mu(v)$ on each that interval can be approximated by its mean value

$$\begin{aligned}\alpha(t_n)&=[1+\nu_0]\mu(t_n)\\&\quad-2\sum_{i=1}^{n}[\mu(t_i)-\mu(t_{i-1})][\nu(t_n-t_i)-\nu(t_n-t_{i-1})].\end{aligned} \tag{A.25}$$

Finally, the new index notation is used for one part of the sum

$$\begin{aligned}&\sum_{i=1}^{n}\nu(t_{i-1})[\nu(t_n-t_i)-\nu(t_n-t_{i-1})]\\&\quad=\sum_{i=0}^{n-1}\mu(t_i)[\nu(t_n-t_{i+1})-\nu(t_n-t_i)]\end{aligned} \tag{A.26}$$

and Eq. (7) turns into

$$\begin{aligned}\alpha(t_n)&=\mu(t_n)[2+\nu_0+\nu(t_n-t_{n-1})]+\mu_0[\nu(t_n)-\nu(t_n-t_1)]\\&\quad+\sum_{i=1}^{n-1}\mu(t_i)[\nu(t_n-t_{i-1})-\nu(t_n-t_{i+1})].\end{aligned} \tag{A.27}$$

An analogous procedure is applied for the transformation of the right-hand side of Eq. (A.20)

$$\mathcal{L}(\beta(t))=3[1-2u\bar{\nu}]\bar{\kappa}, \tag{A.28}$$

which results in the expression

$$\begin{aligned}\beta(t_n)&=3\kappa(t_n)[1-\nu_0-\nu(t_n-t_{n-1})]\\&\quad-3\kappa_0[\nu(t_n)-\nu(t_n-t_1)]\\&\quad-\sum_{i=1}^{n-1}3\kappa(t_i)[\nu(t_n-t_{i-1})-\nu(t_n-t_{i+1})].\end{aligned} \tag{A.29}$$

Now, by using the fact that

$$\mathcal{L}(\alpha(t))=\mathcal{L}(\beta(t))\quad\Rightarrow\quad\alpha(t)=\beta(t), \tag{A.30}$$

the recurrence formula for the current value of the bulk modulus is calculated

$$\begin{aligned}\kappa(t_n)&=\frac{1}{3[1-\nu_0-\nu(t_n-t_{n-1})]}\left[\mu(t_n)[2+\nu_0+\nu(t_n-t_{n-1})]\right.\\&\quad+[\mu_0+3\kappa_0][\nu(t_n)-\nu(t_n-t_1)]\\&\quad\left.+\sum_{i=1}^{n-1}[\mu(t_i)+3\kappa(t_i)][\nu(t_n-t_{i-1})-\nu(t_n-t_{i+1})]\right].\end{aligned} \tag{A.31}$$

Here, the initial value is evaluated according to the standard relationship

$$\kappa_0 = \frac{2\mu_0[1+\nu_0]}{3[1-2\nu_0]}. \tag{A.32}$$

Unlike solution (A.19), the recurrence formula (A.31) can be used for any function defining the change of $\mu(t)$ and $\nu(t)$. It can also be used even if the analytic expressions for these parameters are not given but only the discrete values are available. The procedure can also be applied for the evaluation of another material parameter (i.e. Young's modulus) or if the data on another combination of parameters is known. For example, a common situation is that the data on shear and bulk moduli is available and used for the evaluation of Young's modulus and Poisson's number (Tschoegl, 1989; Kiasat, 2000).

References

Anand, L., Gurtin, M., 2003. A theory of amorphous solids undergoing large deformations, with application to polymeric glasses. Int. J. Solid Struct. 40, 1465–1487.

Boyce, M., Arruda, E., 2000. Constitutive models of rubber elasticity: a review. Rubber Chem. Technol. 73, 504–523.

Feyel, F., 2003. A multilevel finite element method (FE^2) to describe the response of highly nonlinear structures using generalized continua. Comput. Methods Appl. Mech. Eng. 192, 3222–3244.

Feyel, F., Chaboche, J.L., 2000. FE^2 multiscale approach for modelling the elastoviscoplastic behavior of long fibre SiC/Ti composite materials. Comput. Methods Appl. Mech. Eng. 183, 309–330.

Hill, R., 1963. Elastic properties of reinforced solids: some theoretical principles. J. Mech. Phys. Solids 11, 357–372.

Hill, R., 1972. On constitutive macro-variables for heterogeneous solids at finite strain. Proc. R. Soc. Lond. A 326, 131–147.

Hossain, M., Possart, G., Steinmann, P., 2009a. A finite strain framework for the simulation of polymer curing. Part I: Elasticity. Comput. Mech. 44, 621–630.

Hossain, M., Possart, G., Steinmann, P., 2009b. A small-strain model to simulate the curing of thermosets. Comput. Mech. 43, 769–779.

Hossain, M., Possart, G., Steinmann, P., 2010. A finite strain framework for the simulation of polymer curing. Part II. Viscoelasticity and shrinkage. Comput. Mech. 46, 363–375.

Hossain, M., Steinmann, P., 2011. Modeling and simulation of the curing process of polymers by a modified formulation of the Arruda–Boyce model. Arch. Mech. 63 (5–6), 1–13.

Ilic, S., 2010. Manual for the multiscale FE program MSFEAP. <http://www.ruhr-uni-bochum.de/lam/Mitarbeiter/Ilic/index.html>.

Ilic, S., Hackl, K., 2009. Application of the multiscale FEM to the modeling of nonlinear multiphase materials. J. Theor. Appl. Mech. 47, 537–551.

Kiasat, M., 2000. Curing shrinkage and residual stresses in viscoelastic thermosetting resins and composites. Ph.D. Thesis, TU Delft, The Netherlands.

Kiasat, M.S., Marissen, R., 2000. Modelling the cure-dependent viscoelastic behaviour of a thermosetting resin and residual curing stresses. In: Michel, B., Winkler, T., Werner, M., Fecht, H. (Eds.), Proceedings of Third International Micro Materials Conference, MicroMat 2000, Berlin, Germany, Dresden, ddp Goldenbogen, pp. 1063–1066, ISBN 3-932434-15-3.

Klinge, S., Bartels, A., Steinmann, P., 2012. Modeling of curing processes based on a multi-field potential: single and multiscale aspects. Int. J. Solid Struct. http://dx.doi.org/10.1016/j.ijsolstr.2012.04.034.

Klinge, S., Hackl, K., 2012. Application of the multiscale FEM to the modeling of nonlinear composites with a random microstructure. Int. J. Multiscale Comp. Eng. 10 (3), 213–227.

Lion, A., Höfer, P., 2007. On the phenomenological representation of curing phenomena in continuum mechanics. Arch. Mech. 59, 59–89.

Marckmann, G., Verron, E., 2006. Comparison of hyperelastic models for rubber-like materials. Rubber Chem. Technol. 79, 835–858.

Mergheim, J., Possart, G., Steinmann, P., 2012. Modeling and computation of curing and damage of thermosets. Comput. Mater. Sci. 53, 359–367.

Miehe, C., Schröder, J., Bayreuther, C., 2002. On the homogenisation analysis of composite materials based on discretized fluctuations on the microstructure. Acta Mech. 155, 1–16.

Mulliken, A., Boyce, M., 2006. Mechanics of the rate-dependent elastic–plastic deformation of glassy polymers from low to high strain rates. Int. J. Solid Struct. 43, 1331–1356.

O'Brien, D.J., Sottos, N.R., White, S.R., 2007. Cure-dependent viscoelastic Poisson's ratio of epoxy. Exp. Mech. 47, 237–249.

Reese, S., Govindjee, S., 1998. A theory of finite viscoelasticity and numerical aspects. Int. J. Solid Struct. 35, 3455–3482.

Schröder, J., 2000. Homogenisierungsmethoden der nichtlinearen Kontinuumsmechanik unter Beachtung von Stabilitätsoproblemen. Habilitationsschrift, Universität Stuttgart, Deutschland.

Simo, J., Hughes, T.J.R., 1997. Computational Inelasticity. Springer Verlag.

Taylor, R., 2011. FEAP manuals. <http://www.ce.berkeley.edu/projects/feap/>.

Tschoegl, N.W., 1989. The Phenomenological Theory of Linear Viscoelastic Behavior. An Introduction. Springer, Berlin.

Tsou, A.H., Greener, J., Smith, G.D., 1995. Stress relaxation of polymer films in bending. Polymer 36 (5), 949–954.